Novel Fast-Speed Partial-Shading-Tolerant Flexible Power Point Tracking for Photovoltaic Systems with Explicit Key Points Estimation

Yinxiao Zhu, *Graduate Student Member, IEEE,* Huiqing Wen, *Senior Member, IEEE,* Hossein Dehghani Tafti, *Senior Member, IEEE,* Guangyu Wang, *Graduate Student Member, IEEE,* Qinglei Bu, *Member, IEEE,* Guanying Chu, *Member, IEEE,* Haochen Shi, *Member, IEEE,* Yihua Hu, *Senior Member, IEEE,* and Lin Jiang, *Member, IEEE*

***Abstract*—Recent power curtailment-based photovoltaic (PV) flexible power point tracking (FPPT) algorithms mainly adopted intricate curve fitting or sophisticated curve-scanning mechanisms to ensure the grid supportive functionalities under partial shading conditions (PSCs), showing the limitations of mathematical solidity or system dynamics improvement. Accordingly, a novel fast-speed partial-shading-tolerant FPPT (PST-FPPT) algorithm is proposed in this paper. Regarding the proposed scheme, a modified explicit PV model is developed to express the key operation points with the assistance of several representative current-voltage samples from the initialization process, which is beneficial to computational burden reduction and irradiance sensors removal. Additionally, to guarantee the tracking speed to system dynamics, a set point estimation-based direct voltage regulation strategy is proposed in this paper, eliminating the redundant searching in approaching the predefined power command. Simulation and experimental evaluations under various PSCs and operational circumstances validated the effectiveness of the proposed control.**

***Index Terms*—Flexible power point tracking, grid support, key points estimation, partial shading, photovoltaic system.**

Manuscript received XXXX, 2022; revised XXXX, 2023; revised XXXX, 2023; accepted XXXX, 2023. Date of publication XXXX; date of current version XXXX. This work was supported in part by the National Natural Science Foundation of China under Grant 52177195 and Grant 52107212; in part by the Carbon Peak Carbon Neutrality Technology Innovation Programme of Jiangsu Science and Technology Programme Fundamental Research Plan under Grant BK20220029; in part by the Zhejiang Kunpeng Investigator Program; in part by the Suzhou Prospective Application Programme under Grant SYG202016; in part by XJTLU Key Programme Special Fund under Grant KSF-A-08, Grant KSF-E-13, and Grant KSF-T-04; and in part by the Research Development Fund of XJTLU under Grant RDF-22-01-081. (*Corresponding author: Huiqing Wen.*)

Yinxiao Zhu is with the College of Electrical Engineering, Zhejiang University, Hangzhou 310027, China, and was with the Department of Electrical Engineering and Electronics, University of Liverpool, L69 3BX Liverpool, U.K. and the School of Advanced Technology, Xi'an Jiaotong-Liverpool University, Suzhou 215123, China (e-mail: y.zhu@ieee.org).

Huiqing Wen, Guangyu Wang, Qinglei Bu, and Guanying Chu are with the School of Advanced Technology, Xi'an Jiaotong-Liverpool University, Suzhou 215123, China (e-mail: Huiqing.Wen@xjtlu.edu.cn; Guangyu.Wang19@student.xjtlu.edu.cn; Qinglei.Bu02@xjtlu.edu.cn; Guanying.Chu02@xjtlu.edu.cn).

Hossein Dehghani Tafti is with the Department of Electrical, Electronic and Computer Engineering, The University of Western Australia, Perth, WA 6009, Australia (e-mail: hossein002@e.ntu.edu.sg).

Haochen Shi is with the State Key Laboratory of Advanced Electromagnetic Engineering and Technology, School of Electrical and Electronic Engineering, Huazhong University of Science and Technology, Wuhan 430074, China (e-mail: haochenshi@hust.edu.cn).

Yihua Hu is with the Department of Engineering, King's College London, WC2R 2LS London, U.K. (email: yihua.hu@kcl.ac.uk)

Lin Jiang is with the Department of Electrical Engineering and Electronics, University of Liverpool, L69 3BX Liverpool, U.K. (e-mail: l.jiang@liverpool.ac.uk).

Color versions of one or more figures in this article are available at XXXX.

Digital Object Identifier XXXX

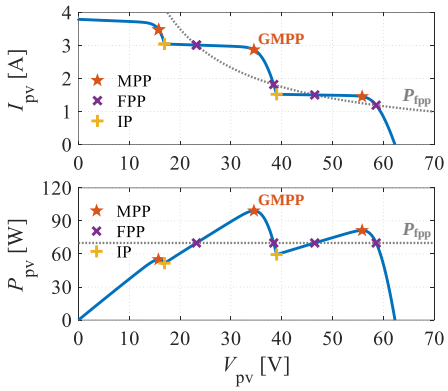

Fig. 1. Flexible power point tracking operation under a indicative PSC. (MPP: maximum power point; FPP: flexible power point; IP: inflection point; GMPP: global MPP; P_{fpp}: external power command from system operators, also the power at FPP)

I. Introduction

RECENTLY, photovoltaic systems (PVSs) are continuously enhancing the penetration level in the power grid, mainly driven by the reduction in manufacture cost [1]. Traditionally, the maximum power point tracking (MPPT) strategy is employed to maximize the power extraction from PVSs [2]. However, the high penetration level of low inertia PVSs integration induced adverse impacts on the stability and quality of power systems, such as voltage fluctuations and frequency bias due to the replacement of traditional synchronous generators [3]–[5]. Accordingly, the concept of flexible power point tracking (FPPT) is developed to fulfill the extended grid support functionalities in revised grid codes and standards [6]–[9] by providing the virtual inertia in PVSs, apart from the conventional MPPT controls [10]–[12]. For instance, the frequency-Watt response is mandatory in revised grid codes or standards like [9], which necessitates FPPT capability.

Generally, the FPPT concept aims to constrain the PV output power to a certain level determined by the operational conditions. There are several solutions to achieve the constraint of the feed-in power of PVSs, such as energy storage systems integration and dump load installation [24]. However, additional hardware raises the capital cost of the power system [25]. Alternatively, power curtailment based on MPPT modification is considered a cost-effective solution for

TABLE I
COMPARISONS BETWEEN VARIOUS FPPT ALGORITHMS

Ref.	Key Features	Operating Region	Complexity	FPP Estimation	Tracking Speed	Shading-Tolerant
[13]	Constant voltage-step	Both	Low	No	Slow	No
[14]	Adaptive voltage-step	Left	Low	No	Medium	No
[15]	Adaptive voltage-step	Left	Low	No	Medium	No
[16]	Binary search	Both	Medium	No	Medium	No
[17]	Model-based approach	Left	Medium	Yes	Fast	No
[18]	Secant-based approach	Both	Low	Yes	Fast	No
[19]	Model-based approach	Right	High	Yes	Fast	No
[20]	Curve fitting-based control	Right	High	No	Fast	Yes
[21]	LMPPs deloading-based control	Both	Low	No	Medium	Yes
[22]	HC&PSO-based control	Left	High	Yes	Medium	Yes
[23]	Curve scanning-based control	Left	Low	No	Slow	Yes
This work	**Explicit model-based approach with direct voltage regulation**	**Left**	**Medium**	**Yes**	**Fast**	**Yes**

approaching FPPT concepts with less additional hardware, which could be mathematically expressed as

$$P_{\rm pv} = \begin{cases} P_{\rm mpp}, & \text{when } P_{\rm avi} \le P_{\rm fpp} \\ P_{\rm fpp}, & \text{when } P_{\rm avi} > P_{\rm fpp} \end{cases} \quad (1)$$

where $P_{\rm mpp}$ is the PV power at maximum power point (MPP), and also the available power $P_{\rm avi}$ of PV string. $P_{\rm fpp}$ is a predetermined power command provided by system operators, also the power at a flexible power point (FPP).

Accordingly, various power curtailment-based FPPT [13]–[19] are introduced in prior art, and the key features of these FPPT methods are summarized and listed in TABLE I. Originated from the conventional perturb and observe (P&O) MPPT strategy, the general FPPT algorithms with constant or adaptive voltage step are proposed in [13]–[15], which ensured the steady-state performance and capability of constant power generation. However, these liner searching-based methods can enhance the effectiveness but are still limited by selecting voltage steps with concerns on balance between tracking speed and accuracy. Different from the solutions above, the work in [16] introduced a binary search-based FPPT algorithm to guarantee tracking speed and steady-state power ripple mitigation with a non-linear searching-based approach. To further improve the tracking speed, the work in [17]–[19] proposed the direct approaches based on the estimation for the corresponding voltage of $P_{\rm fpp}$ command, which could adjust the PV power to the desired level within several iterations. These non-linear searching-based solutions eliminated the dependence on voltage step in conventional liner searching-based methods. However, these methods mainly focus on the uniform irradiance condition, and the partial shading condition (PSC) operation capability should be further addressed [10].

Similarly, the FPPT control is required to move the PV operation point from the global MPP (GMPP) to FPP under PSC. Differential from the uniform irradiance operation, the FPPT operation under PSC becomes more challenging due to the introduction of multiple MPPs, inflection points (IPs), and FPPs in PV output characteristics, as current-voltage (I-V) and power-voltage (P-V) curve, as demonstrated in Fig. 1 [20]. However, only a few works [20]–[23] discussed the challenging FPPT operation under PSC, requiring solid mathematical fundamentals or a sophisticated curve-scanning process. The work in [20] proposed an FPPT algorithm to survive in PSC using the Levenberg-Marquardt-based least-squares curve fitting method to estimate the whole PV output characteristics to approach such key operation points. However, implementing such advanced numerical techniques required a solid mathematical background and enhanced computational complexity, limiting wide applications. Additionally, a scan mode is employed in [20] to scan most of the P-V curve to gain extensive samples for subsequent estimation. Meanwhile, the direct power control at the right-hand side of MPP reduced the robustness, which induced stability concerns under rapidly changing operating conditions [26]. To reduce the computational burden, a power deloading strategy is proposed [21] to obtain the grid support functionalities for PVSs. The deloading region depends on the location of GMPP, where a specific voltage range needs to be scanned to obtain every LMPP. However, such sophisticated searching would dramatically reduce the tracking speed under environmental dynamics. Additionally, if the $P_{\rm fpp}$ command is lower than the power at IP, this method might be trapped in a state with inaccurate deloading power [23]. In [22], a hill-climbing and particle swarm optimization (HC&PSO)-based FPPT control is proposed to increase the tracking speed. However, introducing a PSO-like heuristic algorithm raises concerns about implementation complexity and computational burden. Additionally, the HC&PSO is required to implement extra irradiance and temperature sensors for subsequent calculations. Alternatively, the work in [23] provided a simple solution based on the curve scanning concept for mitigating the computational concerns in prior arts. Generally, this method, namely global FPPT (GFPPT), is required to sample various points from the curve to determine the information of multiple MPPs under PSC. Even though the redundant searching range is deducted, the tracking speed is affected by the unrepresentative samples and the inherent constant voltage-step-based power regulation strategy. To the authors' best knowledge, the state-of-the-art FPPT methods cannot guarantee control effectiveness under PSCs with a sufficient balance between the tracking speed and computational burden.

To fill the research gap, a partial-shading-tolerant FPPT (PST-FPPT) algorithm for photovoltaic systems is proposed in this paper, which guarantees a fast tracking speed and provides a reliable operation under PSCs. The main contributions of the proposed PST-FPPT control are summarized as follows:

- Integration of explicit PV model-based key points estimation strategies for MPPs, IPs, and FPPs.
- Straightforward initialization for current-based PSC detection without sophisticated searching iterations and additional hardware requirements like irradiance sensors.
- Attainment of fast tracking speed by introducing a direct voltage regulation pathway based on the estimation for FPP voltage corresponding to the predefined $P_{\rm fpp}$ command.
- Environmental or operational variations could be detected by monitoring the output power.

Notably, the operation region of the proposed control is allocated on the left-hand side of MPP (LHS-MPP), which ensures robustness [26]. The effectiveness of the proposed PST-FPPT is validated by simulations and experiments under various shading scenarios.

The remainder of this paper is organized as follows. Section II details the proposed PST-FPPT algorithm and the corresponding estimation for key operation points. The simulations and experimental evaluations are provided in Section III and Section IV, respectively. Finally, the conclusions of this work are outlined in Section V.

II. Proposed PST-FPPT Algorithm

Basically, the proposed PST-FPPT is aiming to restrain the PV output power to the $P_{\rm fpp}$ command. As illustrated in Fig. 1, various FPPs can be developed to meet the $P_{\rm fpp}$ command under PSC. In this paper, the FPPs allocated at the left-hand side of MPPs, also the constant current region (CCR), are considered as the recommended operation point, considering the higher stability under system dynamics [26]. Fig. 2 demonstrated the control diagram of the proposed algorithm approach in two-stage grid-connected PVSs. Generally, the two-stage configuration with boost converter-based power interface can extend the operation region of both MPPT and FPPT operations [26]. Meanwhile, the DC-link capacitor decouples the DC power and AC power in a two-stage configuration, which acts as a buffer [27]. Thus, the MPPT and FPPT algorithms can be implemented in the controller of the boost converter to regulate the PV power extraction directly and decoupled with the inverter control. Notably, the proposed method is mainly focused on small-scale PV systems with two-stage configurations, especially distributed PV systems, or an extremely large DC-link capacitor is required if applied to large/utility-scale PV systems.

A. Expressions for Key Operation Points

Considering the multiple peaks in the power-voltage curve under PSC, an effective solution for approaching MPPs and inflection points (IPs) is essential for the FPPT algorithm with shade-tolerant capability. In this paper, an explicit model in [28] is modified to express the MPPs in a partially shaded PV string by using the specifications from the datasheet. Accordingly, the derivation for modeling the entire PV string can be eliminated, reducing the complexity of implementation. According to [28], the expression for the $j^{\rm th}$ MPP of a PV string comprising $N_{\rm m}$ modules with n irradiance levels, $\rm MPP_j$, is mathematically delivered as

$$\begin{cases} V_{\rm mpp,j} = \sum\limits_{i=1}^{j} N_i \left[\frac{G_{\rm pv,j}}{G_{\rm pv,i}} V_{\rm mpp0} + \left(1 - \frac{G_{\rm pv,j}}{G_{\rm pv,i}}\right) V_{\rm oc0}\right] \\ \qquad\qquad - \sum\limits_{i=j+1}^{n} N_i V_{\rm bp} \\ I_{\rm mpp,j} = G_{\rm pv,j} I_{\rm mpp0} \left[1 + \lambda \left(\sum\limits_{i=1}^{j-1} N_i\right) / N_{\rm m}\right] \\ P_{\rm mpp,j} = V_{\rm mpp,j} I_{\rm mpp,j} \end{cases} \tag{2}$$

where $V_{\rm mpp,j}$, $I_{\rm mpp,j}$ and $P_{\rm mpp,j}$ are the MPP voltage, current and power at $\rm MPP_j$, respectively. $G_{\rm pv,i}$ and $G_{\rm pv,j}$ represent the $i^{\rm th}$ and $j^{\rm th}$ irradiance level in a descending order in the PV string, respectively. N_i refers to the number of PV modules at the irradiance level $G_{\rm pv,i}$. $N_{\rm m}$ is the number of PV modules within the PV string. $V_{\rm bp}$ is the voltage drop of the conducting bypass diode. $V_{\rm mpp0}$ and $I_{\rm mpp0}$ are the MPP voltage and current of a PV module at standard test conditions (STC), respectively. $V_{\rm oc0}$ refers to the open-circuit voltage of the PV module at STC. Here, the specifications at STC can be obtained from the datasheet. λ is a empirical coefficient and adopted at 0.06 as a typical value [28]. Accordingly, the maximum available power can be determined by

$$\begin{cases} V_{\rm gmpp} = \underbrace{\arg\max}_{\{V_{\rm mpp,1}, V_{\rm mpp,2}, \ldots, V_{\rm mpp,n}\}} \{P_{\rm mpp,1}, P_{\rm mpp,2}, \ldots, P_{\rm mpp,n}\} \\ I_{\rm gmpp} = \underbrace{\arg\max}_{\{I_{\rm mpp,1}, I_{\rm mpp,2}, \ldots, I_{\rm mpp,n}\}} \{P_{\rm mpp,1}, P_{\rm mpp,2}, \ldots, P_{\rm mpp,n}\} \\ [P_{\rm gmpp}, p] = \max\{P_{\rm mpp,1}, P_{\rm mpp,2}, \ldots, P_{\rm mpp,n}\} \\ G_{\rm pv,p} = \underbrace{\arg\max}_{\{G_{\rm pv,1}, G_{\rm pv,2}, \ldots, G_{\rm pv,n}\}} \{P_{\rm mpp,1}, P_{\rm mpp,2}, \ldots, P_{\rm mpp,n}\} \end{cases} \tag{3}$$

where $V_{\rm gmpp}$, $I_{\rm gmpp}$ and $P_{\rm gmpp}$ represent the voltage, current and power at GMPP, respectively. p is the index of $P_{\rm gmpp}$ in $P_{\rm mpp}$ matrix. $G_{\rm pv,p}$ is the irradiance level of the key moddule corresponding to the GMPP.

Another type of essential point for the FPPT algorithm under PSC is the inflection points, which identified the operation of the PV modules. Considering the bypass diode conduction state under PSCs, the expression for IPs can be approached by modifying the model in [29] as

$$\begin{cases} V_{\rm ip,j} = \sum\limits_{i=1}^{j} N_{\rm i} V_{\rm op,i(i+1)} - \sum\limits_{i=j+2}^{n} N_i V_{\rm bp} \\ \qquad = \sum\limits_{i=1}^{j} N_{\rm i} V_{\rm T} \ln\left(\frac{I_{\rm ph,i} - I_{\rm ph,i+1}}{I_s} + 1\right) - \sum\limits_{i=j+2}^{n} N_i V_{\rm bp} \\ I_{\rm ip,j} = G_{\rm pv,j+1} I_{\rm sc0} \\ P_{\rm ip,j} = V_{\rm ip,j} I_{\rm ip,j} \end{cases} \tag{4}$$

where $I_{\rm sc0}$ is the short circuit current of the PV module at STC, which can be obtained from the datasheet. $V_{\rm ip,i}$, $I_{\rm ip,i}$ and $P_{\rm ip,i}$ are the voltage, current and power at $\rm IP_1$, respectively. Here, $V_{\rm T}$ is the thermal voltage and described as $V_{\rm T} = kT/q$, being k, T, q the Boltzmann's constant, thermodynamic temperature

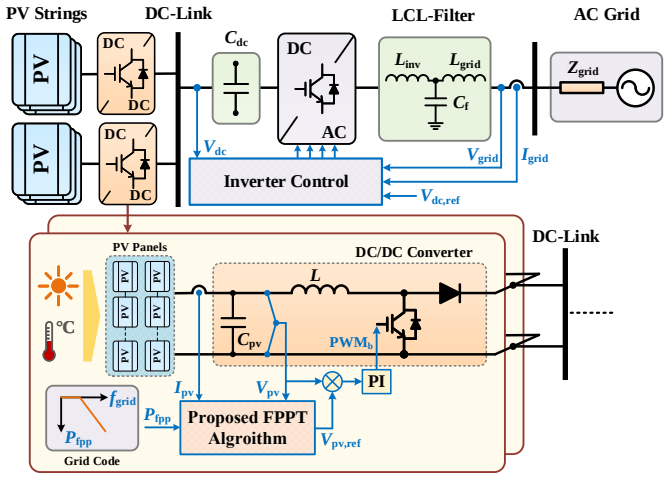

Fig. 2. System configuration and control structure of two-stage grid-connected photovoltaic systems.

TABLE II
SPECIFICATIONS OF THE MSX-60 PV MODULE

Parameter	Symbol	Value
Number of PV cells	$N_{\rm s}$	36
MPP voltage at STC	$V_{\rm mpp0}$	17.1V
MPP current at STC	$I_{\rm mpp0}$	3.5A
MPP power at STC	$P_{\rm mpp0}$	59.85W
Open-circuit voltage at STC	$V_{\rm oc0}$	21.1V
Short-circuit current at STC	$I_{\rm sc0}$	3.8A
Series resistance	$R_{\rm s}$	0.38659Ω
Shunt resistance	$R_{\rm sh}$	161.0752Ω
Temperature coefficient of $V_{\rm oc}$	$\beta_{V_{\rm oc}}$	−80mV/°C
Temperature coefficient of $I_{\rm sc}$	$\beta_{I_{\rm sc}}$	0.065%/°C

and electron charger. $I_{\rm ph,i}$ and $I_{\rm ph,i+1}$ are the photo-current of the PV module at the irradiance level $G_{\rm pv,i}$ and $G_{\rm pv,i+1}$, respectively.

Notably, the number of IPs is one less than the number of irradiance levels in the PV string, as $n-1$ IPs for a PV string with n irradiance levels. The photo-current at irradiance level $G_{\rm pv,i}$ can be rewritten with the introduction of equivalent resistances, which is as

$$I_{\rm ph,i} = G_{\rm pv,i} I_{\rm sc0} \left(1 + \frac{R_{\rm s}}{R_{\rm sh}}\right) \tag{5}$$

where $R_{\rm s}$ and $R_{\rm sh}$ are the equivalent series- and parallel-resistance in PV equivalent model, respectively.

For instance, Fig. 3(a) illustrated a partially shaded PV string formed by three MSX-60 PV modules, which is with three solar irradiance levels $G_{\rm pv,1}$, $G_{\rm pv,2}$ and $G_{\rm pv,3}$. The specification of MSX-60 PV modules are summarized in TABLE II, and the P-V curve under the indicative PSC is demonstrated in Fig. 3(b). Fig. 3(c) illustrated the corresponding I-V characteristics and marked the operation points of each PV module while operating at $\rm MPP_2$. In this case, the PV module $\rm PV_1$ operates at the reduced current $I_{\rm mpp,2}$ dictated by $G_{\rm pv,2}$ of $\rm PV_2$, while $\rm PV_3$ is bypassed. According to (2),

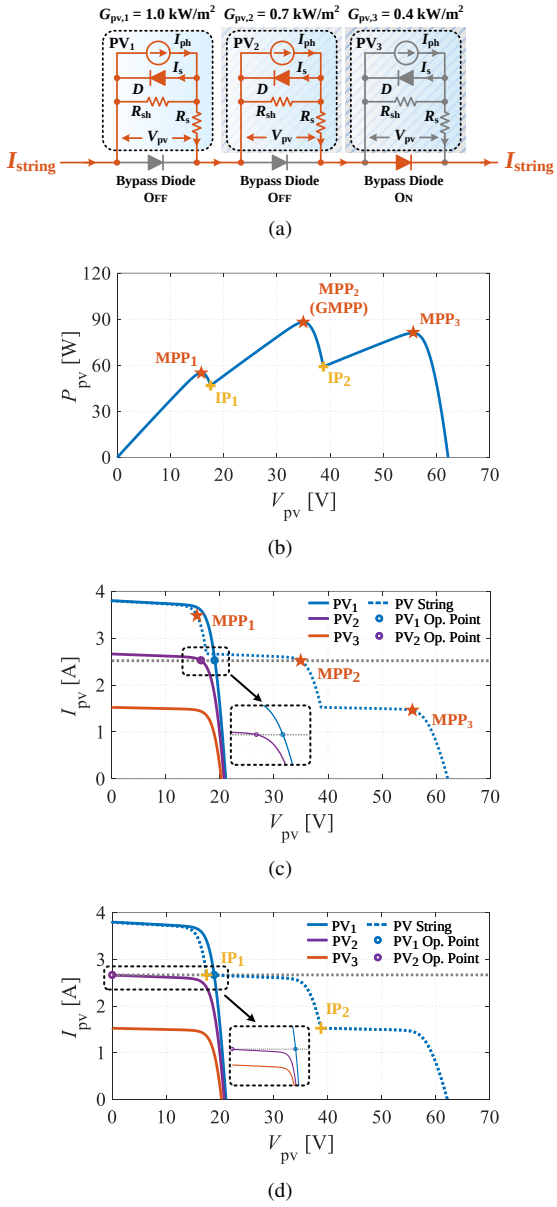

Fig. 3. Output characteristics of a PV string comprising three MSX-60 PV modules under example PSC. (a) Current flow of the PV string operating within the voltage range between $\rm IP_1$ and $\rm IP_2$. (b) Operation points of modules $\rm PV_1$ and $\rm PV_2$ while the string operates at $\rm MPP_2$ with bypassed module $\rm PV_3$. (c) Operation points of modules $\rm PV_1$ and $\rm PV_2$ while the string operates at $\rm IP_1$ with bypassed module $\rm PV_3$.

the expression for $\rm MPP_2$ is delivered as

$$\begin{cases} V_{\rm mpp,2} = N_1 \left[\frac{G_{\rm pv,2}}{G_{\rm pv,1}} V_{\rm mpp0} + \left(1 - \frac{G_{\rm pv,2}}{G_{\rm pv,1}}\right) V_{\rm oc0}\right] \\ \qquad\qquad + N_2 V_{\rm mpp0} - N_3 V_{\rm bp} \\ I_{\rm mpp,2} = G_{\rm pv,2} I_{\rm mpp0} \left[1 + \lambda N_1 / N_m\right] \\ P_{\rm mpp,2} = V_{\rm mpp,2} I_{\rm mpp,2} \end{cases} \tag{6}$$

N_1, N_2 and N_3 are the number of PV modules with irradiance level $G_{\rm pv,1}$, $G_{\rm pv,2}$ and $G_{\rm pv,3}$, respectively. N_1, N_2 and N_3 equal to 1 in this example pattern.

At $\rm IP_1$, the operation stage of the PV string is similar to that at $\rm MPP_2$, which is as shown in Fig. 3(a). Different from the $\rm MPP_2$ operation, PV_1 is operated at the reduced current $I_{\rm ip,1}$ in this condition, while PV_3 is bypassed. According to

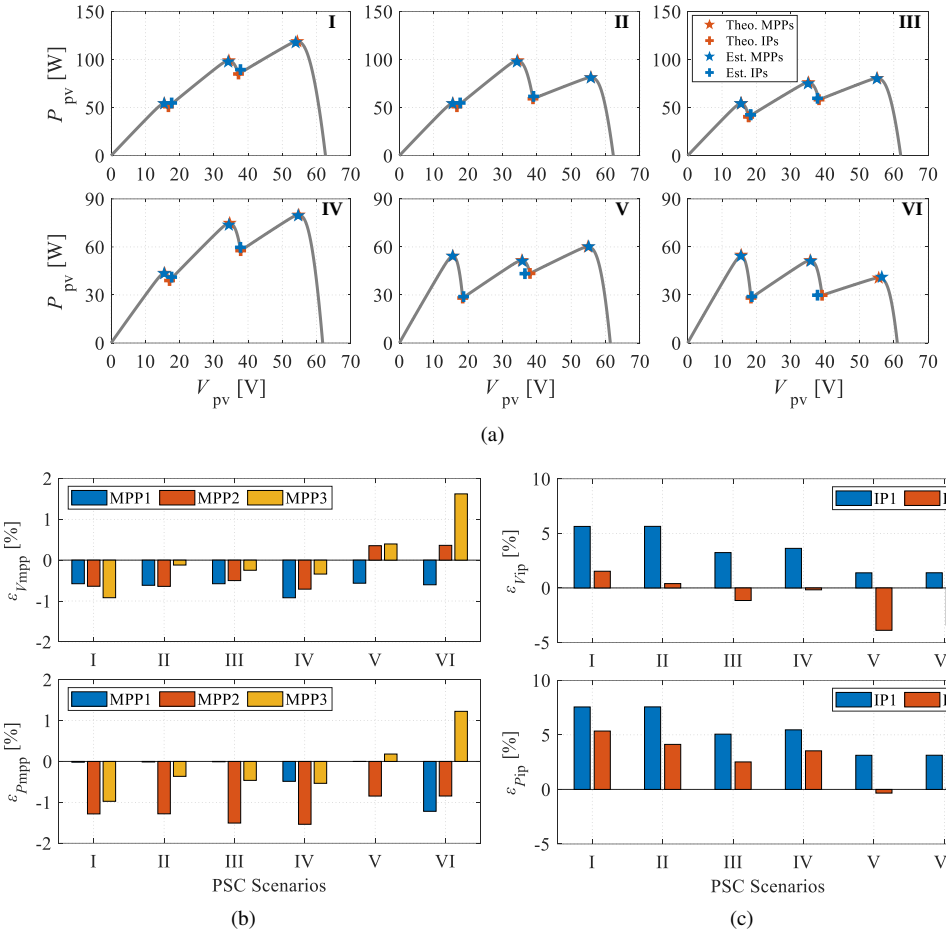

Fig. 4. Estimation accuracy analysis for the modified explicit PV model. (a) Example PSCs with theoretical and estimated points. (b) Estimation error at MPPs. (c) Estimation error at IPs.

(4) and (5), the expression for IP_1 is delivered as

$$\begin{cases} V_{\mathrm{ip},1} = N_1 V_{\mathrm{T}} \ln\left[\frac{I_{\mathrm{sc0}}(G_{\mathrm{pv},1}-G_{\mathrm{pv},2})\left(1+\frac{R_{\mathrm{s}}}{R_{\mathrm{sh}}}\right)}{I_s}+1\right] - N_3 V_{\mathrm{bp}} \\ I_{\mathrm{ip},1} = G_{\mathrm{pv},2} I_{\mathrm{sc0}} \\ P_{\mathrm{ip},1} = V_{\mathrm{ip},1} I_{\mathrm{ip},1} \end{cases} \tag{7}$$

The rest of MPPs and IPs can be expressed in the same process.

Fig. 4 analyzed the accuracy of estimated MPPs and IPs by using the modified explicit PV model under various indicative PSCs. Fig. 4(a) illustrated the theoretical and estimated MPPs and IPs. Then, the numerical comparisons are demonstrated in Fig. 4(b) and Fig. 4(c) in terms of voltage error at MPPs $\varepsilon_{V_{\mathrm{mpp}}}$, power error at MPPs $\varepsilon_{P_{\mathrm{mpp}}}$, voltage error at IPs $\varepsilon_{V_{\mathrm{ip}}}$, and power error at IP $\varepsilon_{P_{\mathrm{ip}}}$. Regarding the MPPs, the estimation errors can be restrained within $\pm 2\%$ by employing the modified explicit model, which is reasonable. Meanwhile, the estimation errors at IPs can be effectively limited to an acceptable range for subsequent FPP estimation.

B. Estimation for Key Operation Points

The irradiance sensors are required to measure the meteorological data from corresponding PV modules while using the above expressions directly. However, the extra sensors will further enhance the system implementation cost, reducing cost-effectiveness. To address this issue, a key points estimation procedure is proposed with the current-based irradiance estimation in this paper.

The proposed estimation involves collecting a set of voltages and currents from the LHS-MPP, which is also the constant current region (CCR) of each PV module. Notably, each voltage and current pair is from a different PV module, that is, N_{m} initial samples are required for applying in a PV string with N_{m} modules. At the CCR region, the dI/dV slope is approximated to zero, and dP/dV is much lower than that at the right-hand side of MPP (RHS-MPP) [17], [30], [31]. Compared with operating at RHS-MPP, the LHS-MPP operation guarantee higher operational stability under the rapid-changing environmental conditions [26]. Accordingly, the irradiance estimation can be developed for the samples from the LHS-MPP region to eliminate the aid of irradiance sensors, which is cost-effective.

Based on the PV string comprising three modules, the proposed estimation procedure for key operation points is shown in Fig. 5. Firstly, the PV currents at CCR are collected from initial voltages by implementing an initialization process.

Here, the $n_{\mathrm{init}}{}^{\mathrm{th}}$ initial voltage, $V_{\mathrm{pv},\mathrm{n_{init}}}$, is expressed as

$$V_{\mathrm{pv},\mathrm{n_{init}}} = [\sigma_{\mathrm{ccr}} + \sigma_{\mathrm{eq}}(n_{\mathrm{init}}-1)]V_{\mathrm{oc0}} - (N_{\mathrm{m}} - n_{\mathrm{init}})V_{\mathrm{bp}} \tag{8}$$

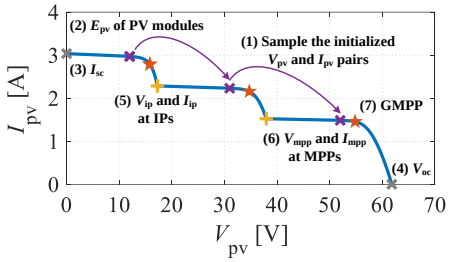

Fig. 5. Estimation procedure for key operation points.

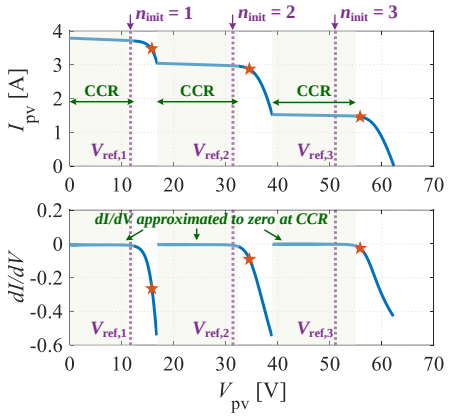

Fig. 6. Current-voltage curve and dI/dV curve of a PV string comprising three modules with initial voltage lines.

$\sigma_{\rm ccr}$ is a coefficient set at 0.65 to guarantee the CCR operation during the initialization, $\sigma_{\rm eq}$ is the approximated equivalent operation voltage of PV module, and $n_{\rm init} \in [1, N_{\rm m}]$. Fig. 6 illustrated the allocation of initial voltage lines under an example PSC. The initial voltage lines are allocated in the CCR according to (8), where dI/dV is approximately equal to zero. Subsequently, the initial current samples will be sorted in descending order. Considering the near-zero dI/dV at CCR, the ${n_{\rm init}}^{\rm th}$ irradiance level in initialization process $G_{\rm pv,n_{init}}$ can be estimated by

$$G_{\rm pv,n_{init}} = \frac{I_{\rm pv,n_{init}}}{I_{\rm sc0}} \tag{9}$$

where $I_{\rm pv,n_{init}}$ is the ${n_{\rm init}}^{\rm th}$ PV currents of the $N_{\rm m}$ initial samples in descending sort. Similarly, the irradiance levels of all modules can be estimated by using (9). Fig. 7 illustrated the impact of different equivalent $V_{\rm pv,n_{init}}$ and environmental conditions on the accuracy of irradiance estimation. Generally, as demonstrated in Fig. 6, dI/dV is approximated to zero at CCR. Accordingly, the impact of the variation of $V_{\rm pv,n_{init}}$ on the irradiance estimation error $\varepsilon_{G_{\rm pv}}$ is ignorable. Regarding the environmental variations, the $\varepsilon_{G_{\rm pv}}$ diversion is more sensitive to to temperature variations than irradiance. That is, the absolute $\varepsilon_{G_{\rm pv}}$ is restricted to an acceptable range, as $\pm 5\%$, under investigated extreme conditions with the $V_{\rm pv,n_{init}}$. Notably, the estimation accuracy using (9) can be enhanced by implementing the temperature sensors but increases the system cost.

To be noticed, the corresponding PV modules will be considered at the same irradiance level for simplification if the absolute current difference between two initialized samples is no more than 0.1. Then, the initial $G_{\rm pv}$ matrix, the number

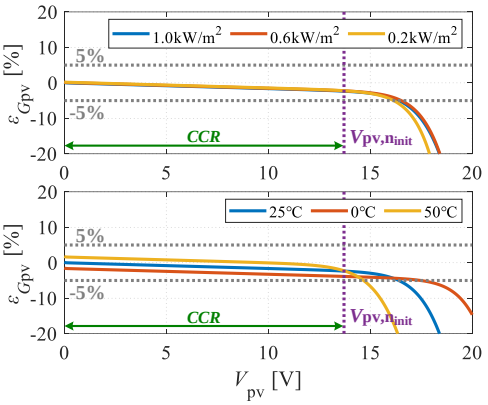

Fig. 7. Impact of equivalent $V_{\rm pv,n_{init}}$ differences and environmental variations on the estimation for irradiance.

of total irradiance levels n and the number of modules with the $G_{\rm pv,i}$ irradiance level $N_{\rm i}$ are determined. Subsequently, the string-level short circuit current $I_{\rm sc}$ is determined by the PV modules with the highest irradiance level $G_{\rm pv,1}$ and expressed as

$$I_{\rm sc} = G_{\rm pv,1} I_{\rm sc0} \tag{10}$$

and the string-level open-circuit voltage can be delivered as

$$V_{\rm oc} = \sum_{i=1}^{n} N_{\rm i} V_{\rm oc,i} \cong \sum_{i=1}^{n} N_{\rm i} N_{\rm s} \alpha \ln\left(\frac{I_{\rm sc,i}}{I_{\rm s}} + 1\right) \tag{11}$$

where $V_{\rm oc,i}$ is the open-circuit voltage of a PV module at the irradiance $G_{\rm pv,i}$. $N_{\rm s}$ and α represent the number of series-connected PV cells and modified diode ideal factor in a PV module, respectively. Then, the inflection points, IPs, can be obtained by combining (4) and (5). Subsequently, the MPPs and GMPP can be approached by (2) and (3). The proposed estimation process for the key operation points with an initialization procedure is completed here. The rest of the proposed PST-FPPT algorithm is developed from this estimation process.

C. Proposed PST-FPPT Algorithm

The flowchart of the proposed PST-FPPT algorithm for PSCs is as illustrated in Fig. 8, including five control blocks, as GMPPT, FPPT, FPP estimation, initialization, and PSC change detection blocks. Generally, the main control blocks of the proposed algorithm are the GMPPT block and FPPT block, determining the objectives of voltage regulation. Basically, the proposed PST-FPPT aims to restrain the PV output power to the $P_{\rm fpp}$ command by regulating the PV operation point to robust CCR. However, the CCR operation introduces concerns about performance deterioration under system dynamics, such as environmental variations and power command regulation, due to the slight dP/dV slope in this region. Accordingly, an FPP estimation block, as the ancillary path, is proposed to strengthen the dynamic response with CCR operation. Meanwhile, the PSC change detection and initialization blocks are used to update the shading scenarios during the operation. Here, $n_{\rm init}$ is considered a counter for initialization. $S.S.$ represents the operation state, as one refers to steady-state and zero refers to dynamic. $S._{\rm fpp}$ is adopted to trigger the direct FPP path, where one is for activation and zero is for dormancy.

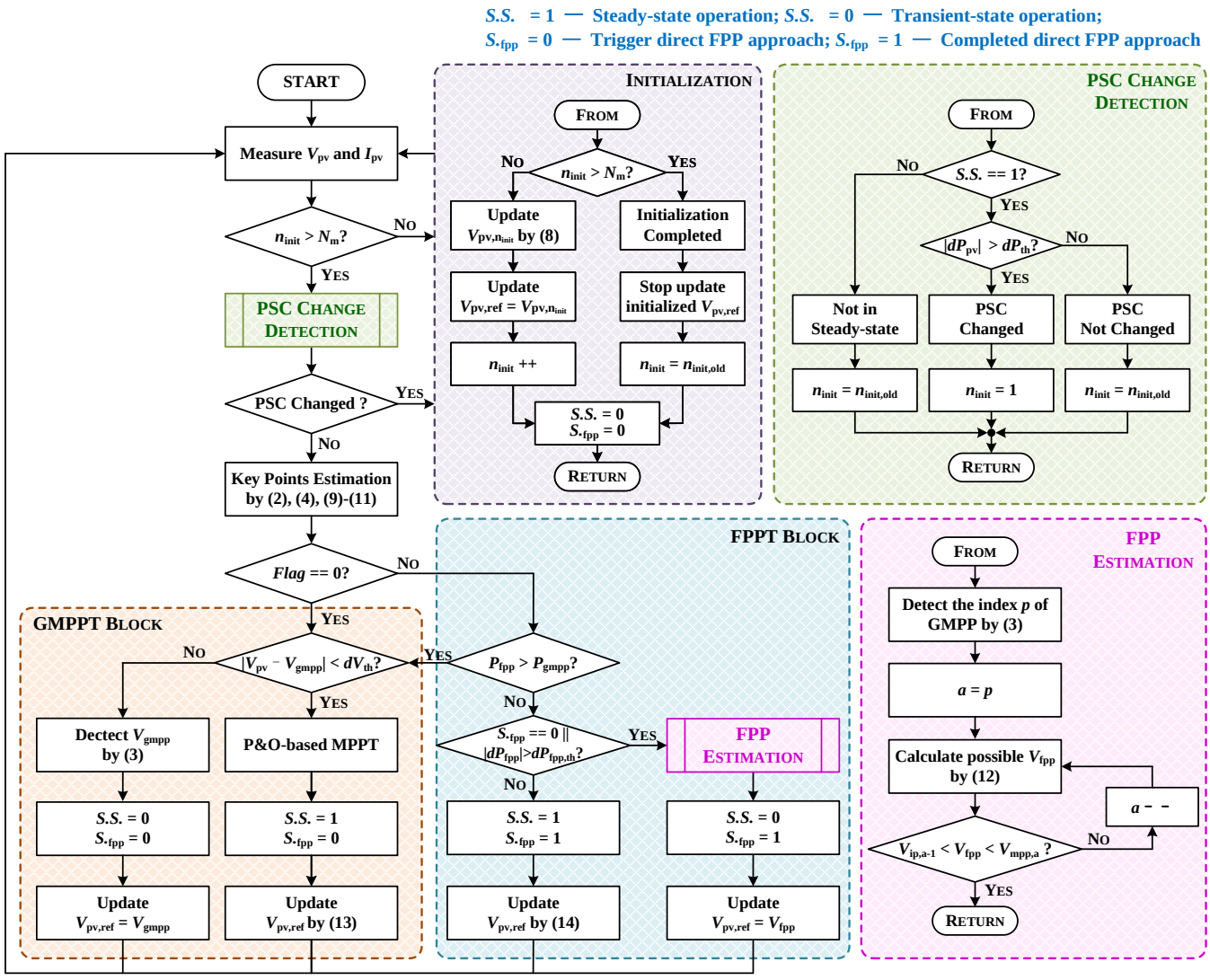

Fig. 8. Flowchart of the proposed PST-FPPT algorithm.

1) Initialization Block: Basically, the initialization block is adopted to obtain the information from representative voltages at CCR, which is essential for subsequent estimation. Initially, $n_{\rm init}$ is set to 1 and the representative points will be recorded from the left-most peaks according to the initialized voltage set by using (8). Then, the value of $n_{\rm init}$ will be added one and recorded the information at subsequent $V_{{\rm pv},n_{\rm init}}$. Once $n_{\rm init}$ is larger than $N_{\rm m}$, all representative points are obtained, and the initialization process is considered completed and stops the update of $V_{{\rm pv},n_{\rm init}}$. In this block, $S.S.$ and $S._{\rm fpp}$ are continuously set at zero.

2) FPP Estimation Block: To guarantee the tracking speed, an FPP estimation block is developed to estimate the corresponding FPP voltage of the $P_{\rm fpp}$ command in the proposed PST-FPPT algorithm. According to the current-voltage pairs from the initialization process, the index p corresponding to the GMPP in the initialized samples can be determined. Then, assigning p to a, the FPP voltage $V_{\rm fpp}$ at CCR can be calculated by

$$V_{\rm fpp} = \frac{P_{\rm fpp}}{G_{{\rm pv,a}} I_{\rm sc0}} \tag{12}$$

Notably, only $V_{{\rm ip,a}-1} < V_{\rm fpp} < V_{\rm mpp,a}$ is considered as the sign of completing FPP estimation, and the value of $V_{\rm fpp}$ can be adopted as the voltage reference for enhancing the tracking speed. Otherwise, the value of a will be deducted one, and $V_{\rm fpp}$ is recalculated by (12) to approach the potential FPP according to the value of $G_{{\rm pv,a}-1}$. Meanwhile, the $V_{\rm fpp}$ with (12) is only available for using the initialized voltage set from the CCR according to the proportionality between the irradiance and short-circuit current at STC.

3) PSC Change Detection Block: In this algorithm, a PSC change detection block is introduced to detect the irradiance variations during operation. Generally, if $S.S.$ is equal to zero, the operation is considered not in the steady state, then, $n_{\rm init}$ is not changed. Alternatively, the irradiance variation is detected if the absolute value of $dP_{\rm pv}$ is greater than the predefined threshold $dP_{\rm th}$. Then, $n_{\rm init}$ is reset to one, and the initialization is triggered again.

4) Main Control Scheme: Generally, the proposed control is required to measure the PV voltage and current at every sampling interval. Then, if $n_{\rm init}$ is smaller than the number of PV modules $N_{\rm m}$, the initialization block will be woken up to

record the representative points by using (8). Otherwise, the PSC detection block will be triggered to detect the variation of the shading scenario. If PSC is changed, the initialization block will be re-triggered, or, the key point estimation progress will be enabled. Then, the irradiance level at each module can be estimated by substituting the set of initialized voltage-current pairs to (9). Then, the MPPs and IPs can be obtained by using (2) and (4), respectively. Subsequently, if $Flag$ is equal to zero, the GMPPT block will be triggered to approach the GMPP. If the absolute difference between recent PV voltage $V_{\rm pv}$ and the estimated GMPP voltage $V_{\rm gmpp}$ is greater than the predefined threshold $dV_{\rm th}$, the voltage at GMPP will be directly developed to the voltage reference for fast GMPP approach, and $S.S.$ and $S._{\rm fpp}$ is maintained at zero. Otherwise, the P&O-based MPPT will be triggered to track the GMPP, and $V_{\rm pv,ref}$ is updated by using

$$V_{\rm pv,ref} = \begin{cases} V_{\rm pv,ref,old} + {\rm sgn}(dV_{\rm pv})V_{\rm step}, & dP_{\rm pv} > 0 \\ V_{\rm pv,ref,old} - {\rm sgn}(dV_{\rm pv})V_{\rm step}, & dP_{\rm pv} < 0 \end{cases} \tag{13}$$

where $V_{\rm pv,ref,old}$ is the reference voltage in the last perturbation interval, and $V_{\rm step}$ is the optimal voltage step-size for steady-state operation. Meanwhile, $S.S.$ is switched to one for flagging the steady-state operation, and $S._{\rm fpp}$ is maintained at zero. Notably, in this mode, the embedded GMPPT algorithm can be replaced by other advanced controls like [32]–[34] with an introduction of the $S.S.$ and $S._{\rm fpp}$ for compatibility guarantee.

If $Flag$ is equal to one, the FPPT block will be triggered to restrict the PV output power according to the $P_{\rm fpp}$ command. If $P_{\rm fpp}$ command is larger than the available power $P_{\rm gmpp}$, the GMPPT block will be triggered again to maximize the power extraction from the PV string. Otherwise, the FPP estimation block will be triggered if $S._{\rm fpp}$ equal to zero or the absolute difference between two $P_{\rm fpp}$ command $dP_{\rm fpp}$ is greater than the predefined threshold $dP_{\rm fpp,th}$; then, estimated $V_{\rm fpp}$ will be adopted as the reference voltage to ensure the fast tracking to the $P_{\rm fpp}$ command. If so, $S.S.$ is switched to zero, and $S._{\rm fpp}$ is one. If $S._{\rm fpp}$ equal to one or $|dP_{\rm fpp}|$ is no larger than $dP_{\rm fpp,th}$, the regulation of voltage reference is according to

$$V_{\rm pv,ref} = V_{\rm pv,ref,old} - {\rm sgn}(P_{\rm pv} - P_{\rm fpp})V_{\rm step} \tag{14}$$

In this case, $S.S.$ and $S._{\rm fpp}$ are equal to one.

To visualize the operation of the proposed PST-FPPT algorithm, Fig. 9 illustrated the trajectory of PV operation points under various example conditions, including the PSC variation and $P_{\rm fpp}$ command regulation. The operation trajectory of the proposed PST-FPPT algorithm under the decreased irradiance and constant $P_{\rm fpp}$ command is depicted in Fig. 9(a). Initially, the PV operation point is allocated at Point A to match $P_{\rm fpp}$ power extraction, then shifted to Point A' once the PSC varies. The PV voltage and current will be updated at the following sampling interval, and the PSC change detection subroutine will detect the PSC variation. Then, the initialization process will be triggered, and the initial voltage-current pairs will be sampled from Points B, C, and D in subsequent sampling intervals. Subsequently, the key operation points, as MPPs and IPs, are estimated by employing (2), (4) and (9) to (11). Then,

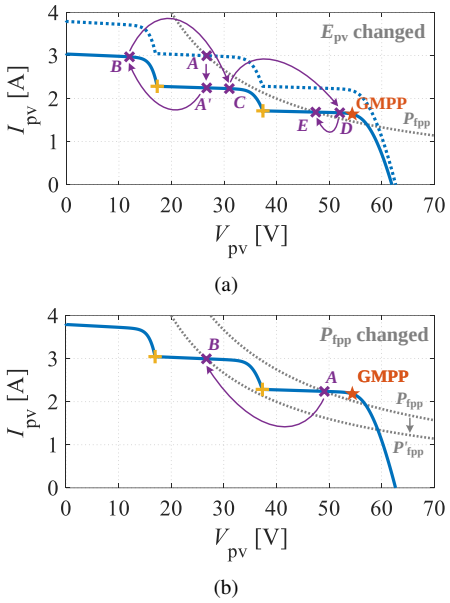

Fig. 9. Trajectory diagram of proposed PST-FPPT algorithm under exemplified conditions. (a) Irradiance variation. (b) $P_{\rm fpp}$ command variation.

the $V_{\rm fpp}$ estimation subroutine is developed to generate the reference voltage to directly approach FPP at the incoming perturbation interval. The operation point will be directly regulated to Point E from D, guaranteeing the tracking speed. After that, the operation will be based on the steady-state regulation strategy in (14).

Fig. 9(b) demonstrated the PV operation trajectory with proposed PST-FPPT algorithm when $P_{\rm fpp}$ command regulated. Initially, the operation point is allocated at Point A with the desired $P_{\rm fpp}$ command. Subsequently, the $P_{\rm fpp}$ command decreased to $P'_{\rm fpp}$, and the FPP estimation subroutine will be triggered to update the PV reference voltage. Then, the operation point will be moved to Point B directly in the next perturbation interval. Thus, the dynamic response to the PSC or $P_{\rm fpp}$ command variation could be guaranteed by the proposed PST-FPPT algorithm.

D. Design Considerations of the PST-FPPT Scheme

To implement the proposed PST-FPPT control, the design for control parameters should be considered as follows.

1) Perturbation Interval: Generally, the selection of perturbation interval $T_{\rm p}$, also the sampling interval, is required to ensure the period between two successive perturbations is longer than settling time T_ε of $P_{\rm pv}$ transient [31]. Considering the CCR operation in the proposed PST-FPPT control, the perturbation interval $T_{\rm p}$ should be obtained [31]

$$T_{\rm p} \geq T_\varepsilon \simeq -\frac{1}{\zeta \cdot \omega_n} \cdot \ln\left(\varepsilon\sqrt{1-\zeta^2}\right) \tag{15}$$

where nature frequency $\omega_n = 1/\sqrt{L \cdot C_{\rm pv}}$, damping factor $\zeta = 1/(2 \cdot R_{\rm pv}) \cdot \sqrt{L \cdot C_{\rm pv}}$, and $\varepsilon = 0.1$ is chosen. Notably, the perturbation frequency is usually set to 1-10Hz in commercial PVSs and could be directly adopted in the FPPT operation as in [15].

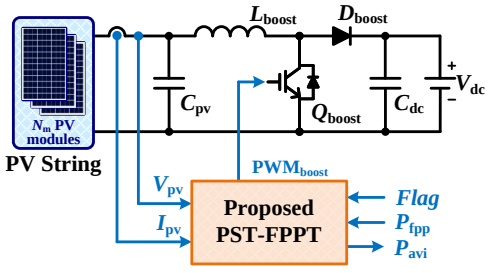

(a)

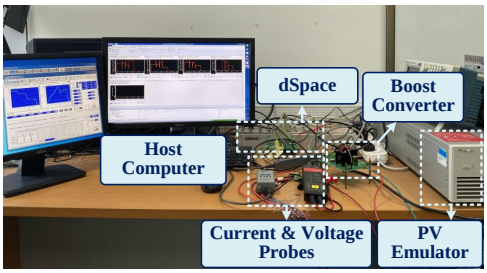

(b)

Fig. 10. (a) Simplified boost converter-based PV system with the proposed control. (b) Experimental prototype.

2) Selection of V_{step}: Here, V_{step} is the optimal voltage step for the MPPT operation. The value of V_{step} could be designed following the classic literature like [35] based on the voltage and power rating of the PVSs.

3) Preset Thresholds: The preset thresholds dP_{th}, $dP_{\text{fpp,th}}$ and dV_{th} are set at 3% to 5% of P_{pv}^{t-1}, 3% to 5% of P_{fpp}^{t-1} and 0.5V, respectively. Here, P_{pv}^{t-1} and P_{fpp}^{t-1} are the PV power and P_{fpp} command in the last perturbation interval, respectively.

4) Enabling Signal: Generally, the enabling signal *Flag* for mode transient is triggered by grid condition in practical operation. For instance, for frequency support, the FPPT mode is required to be activated when the frequency exceeds the nominal range. Then, the FPPT operation is disabled once the frequency is returned to a steady state.

5) DC-link Capacitance: Basically, in this method, the DC-link capacitor is required to act as an energy buffer and assist in DC-link voltage maintenance during the initialization process. Accordingly, considering the requirement on the ripple on DC-link voltage Δv during normal operation, the design for DC-link capacitance C_{dc} should follow [27]

$$C_{\text{dc}} = \frac{P_{\text{pv}}}{(2\pi f_g) \cdot \Delta v \cdot v_{\text{dc}}} \tag{16}$$

where f_g and v_{dc} are the grid frequency and DC-link voltage, respectively. Notably, the increment of DC-link capacitance can contribute to voltage ripple mitigation, degrading the cost-effectiveness and reliability [36]. Meanwhile, increasing the PV string length may dramatically increase the required DC-link capacitance while adopting the proposed methods. Accordingly, the proposed scheme is more suitable for small-scale PV applications.

III. Simulation Evaluation

The effectiveness of the proposed PST-FPPT algorithm is validated with a simplified boost converter-based PVS, as demonstrated in Fig. 10(a), and the system specifications are listed in TABLE III. The PV string consists of three series-connected MSX-60 PV modules, and the MSX-60 PV module specifications are listed in TABLE II. Here, the sampling interval T_{p} is selected at 0.1s to reduce the required time for simulation. Meanwhile, indicative three-peaks shading scenarios with different characteristics, as illustrated in Fig. 11, are employed in this section, and the irradiance levels of each module are listed as

- Case 3-peaks-I: 1.0kW/m^2, 0.8kW/m^2, 0.6kW/m^2
- Case 3-peaks-II: 1.0kW/m^2, 0.8kW/m^2, 0.4kW/m^2
- Case 3-peaks-III: 1.0kW/m^2, 0.4kW/m^2, 0.3kW/m^2
- Case 3-peaks-IV: 1.0kW/m^2, 0.4kW/m^2, 0.2kW/m^2

The maximum power extraction of three cases are 118.8W, 99.18W, 60.3W, and 54.91W, respectively.

TABLE III
Specifications of the Simplified PVS and the Proposed Control

Parameter	Symbol	Value
Input capacitor	C_{pv}	470 μF
Output capacitor	C_{dc}	47 μF
Inductor	L_{boost}	1 mH
Power switch	Q_{boost}	IRG4PH50U
Diode	D_{boost}	RHRG30120
Switching frequency	f_{sw}	20 kHz
Output voltage	V_{dc}	80 V
Sampling interval (Sim.)	T_{p}	0.1 s
Sampling interval (Exp.)	T_{p}	0.3 s
Threshold	dP_{th}	3% P_{pv}^{t-1}
Threshold	$dP_{\text{fpp,th}}$	3% P_{fpp}^{t-1}
Threshold	dV_{th}	0.5 V

*Sim. - Simulation; Exp. - Experiment

A. Steady Three-Peaks Shading Scenarios

Fig. 12 demonstrated the simulation results of the proposed FPPT algorithm under the investigated three-peaks PSCs, and the corresponding trajectories are illustrated in Fig. 13. Initially, the P_{fpp} command is set at 100W and reduced to 80W at time instant $t_3 = 1$s. Meanwhile, the proposed FPPT algorithm is activated at the time instant $t_0 = 0.2$s. $Flag$ is initially set at one to provide the operation at FPPT mode. At time instant $t_5 = 1.6$s, $Flag$ will be regulated to zero, and the proposed PST-FPPT will be operated at MPPT mode.

Fig. 12(a) and Fig. 13(a) illustrated the simulation results and operational trajectory of the proposed PST-FPPT algorithm under the shading scenario Case 3-peaks-I, respectively. The proposed algorithm is enabled at time instant t_0, and the initialization procedure is activated to ensure the representative voltage-current pairs for detecting the shading conditions, following arrows a, b and c. The initialization process is completed at t_1, and the MPPs, IPs, I_{sc}, and V_{oc} are obtained by the proposed key points estimation strategy. In this case, the P_{gmpp} value is larger than that of P_{fpp} command. Thus, the PV operation point is regulated to the FPP to approach the P_{fpp} (following arrow d) by employing the FPP estimation subroutine at time instant t_1. Subsequently, the P_{pv} regulation is based on (14) till the P_{fpp} command changed at time instant t_3. At time instant t_3, the P_{fpp} command is reduced to 80W,

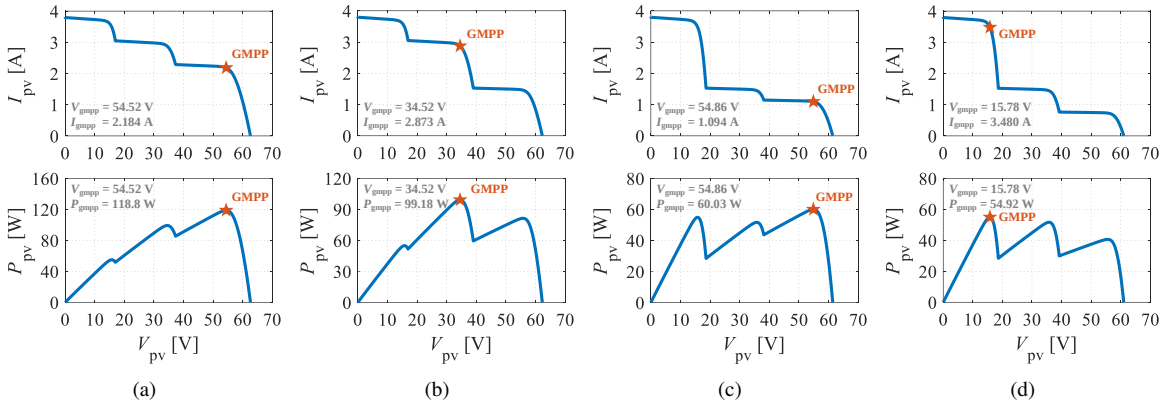

Fig. 11. Theoretical PV output characteristics under various three-peaks PSCs. (a) Case 3-peaks-I. (b) Case 3-peaks-II. (c) Case 3-peaks-III. (d) Case 3-peaks-IV.

and the estimation of $V_{\rm fpp}$ is triggered again. The voltage reference is updated with the new $P_{\rm fpp}$ command based on the result of $V_{\rm fpp}$ estimation in the subsequent perturbation interval (following arrow *e*). Then, reference voltage regulation is according to (14) since t_4. At time instant t_5, the *Flag* is switched to zero, and the proposed PST-FPPT algorithm is required to operate in MPPT mode. The operation point is switched to the estimated GMPP from the FPP (following arrow *f*) at the incoming perturbation interval to guarantee a high tracking speed with mode transition. The tracking point will be the GMPP for the rest of the time.

Fig. 12(b) demonstrated the simulation results under Case 3-peaks-II, and the corresponding trajectory is shown in Fig. 13(b). The available power at GMPP is 99.18W, which is lower than the initial $P_{\rm fpp}$ command. In this case, since the initialization (following arrows *a*, *b* and *c*) is completed, the proposed algorithm is required to maximize the power extraction by employing the internal MPPT operation (following arrow *d*) when the $P_{\rm fpp}$ command is 100W. At time instant t_3, the operation point of PV string is switched to FPP from GMPP following the arrow *e* to curtail the power extraction, considering $P_{\rm fpp}$ command is reduced to 80W and it is larger than the available power. Then, the operation point is maintained at around the FPP to match the $P_{\rm fpp}$ constraint. At time instant t_5, the operation point is returned to GMPP following arrow *f* to maximize the PV output power due to the mode transition.

The simulation results and operational trajectory corresponding to Case 3-peaks-III are illustrated in Fig. 12(c) and Fig. 13(c), respectively. Unlike Case 3-peaks-I and 3-peaks-II, the available power $P_{\rm gmpp}$ is kept lower than the $P_{\rm fpp}$ command during the whole simulation. Thus, the proposed PST-FPPT algorithm must operate in the internal MPPT mode (following the arrow *d*) within the FPPT mode since the initialization is completed at t_1. The *Flag* is set to zero at time instant t_5, and the operation is switched to MPPT mode to extract the available power.

Similarly, under Case 3-peaks-IV, the operation point is continuously allocated at GMPP due to available power $P_{\rm gmpp}$ is constantly lower than the $P_{\rm fpp}$ command, as shown in Fig. 12(d) and Fig. 13(d).

B. Dynamic Three-Peaks Shading Scenarios

The simulation results and corresponding trajectory of the proposed scheme under dynamic PSCs are demonstrated in Fig. 14 and Fig. 15, respectively. The PSCs transition has followed the trajectory of Case 3-peaks-I $\rightarrow$ Case 3-peaks-II $\rightarrow$ Case 3-peaks-III $\rightarrow$ Case 3-peaks-IV. The proposed PST-FPPT algorithm is enabled at t_0. The *Flag* signal is constantly maintained at 1. Meanwhile, the $P_{\rm fpp}$ command is continuously maintained at 90W during the whole simulation.

Similarly, the initialization process detects the shading condition after activating the proposed PST-FPPT algorithm at time instant t_0. Then, the operation point is regulated to the FPP based on the FPP estimation strategy (following arrow *a*) and maintained at the predefined $P_{\rm fpp}$ command till the PSC is changed to Case 3-peaks-II at time instant t_2 (following arrow *b*). Once the PSC variation is detected, the initialization procedure is reactivated to update the PSC information. Subsequently, the available power of Case 3-peaks-II will be updated by combining the representative samples with key point estimation (following arrow *c*). The PV power extraction is successfully constrained at the recommended level, considering $P_{\rm gmpp}$ with Case 3-peaks-II is larger than the predefined $P_{\rm fpp}$ command. At time instant t_4, the shading scenario is varied to Case 3-peaks-III (following arrow *d*), and the initialization is enabled once again. In this case, the estimated available power $P_{\rm gmpp}$ is lower than the $P_{\rm fpp}$ command. Thus, after completing the initialization, the proposed algorithm directly switches the operation point to the GMPP (following arrow *e*) and operates at the internal MPPT mode to fully extract the available power at GMPP. At time instant t_5, the shading scenario is transited to Case 3-peaks-IV (following arrow *f*). Similarly, the operation point is directly allocated at the GMPP once initialization is finished (following arrow *g*). Subsequently, the maximum power extraction is maintained by the internal MPPT operation.

C. Comparison with Other FPPT Controls

To further validate the control advances of the proposed algorithm, three representative FPPT controls are repeated for a fair comparison under dynamic PSCs, including the conventional FPPT in [13], Secant-based FPPT in [18], and

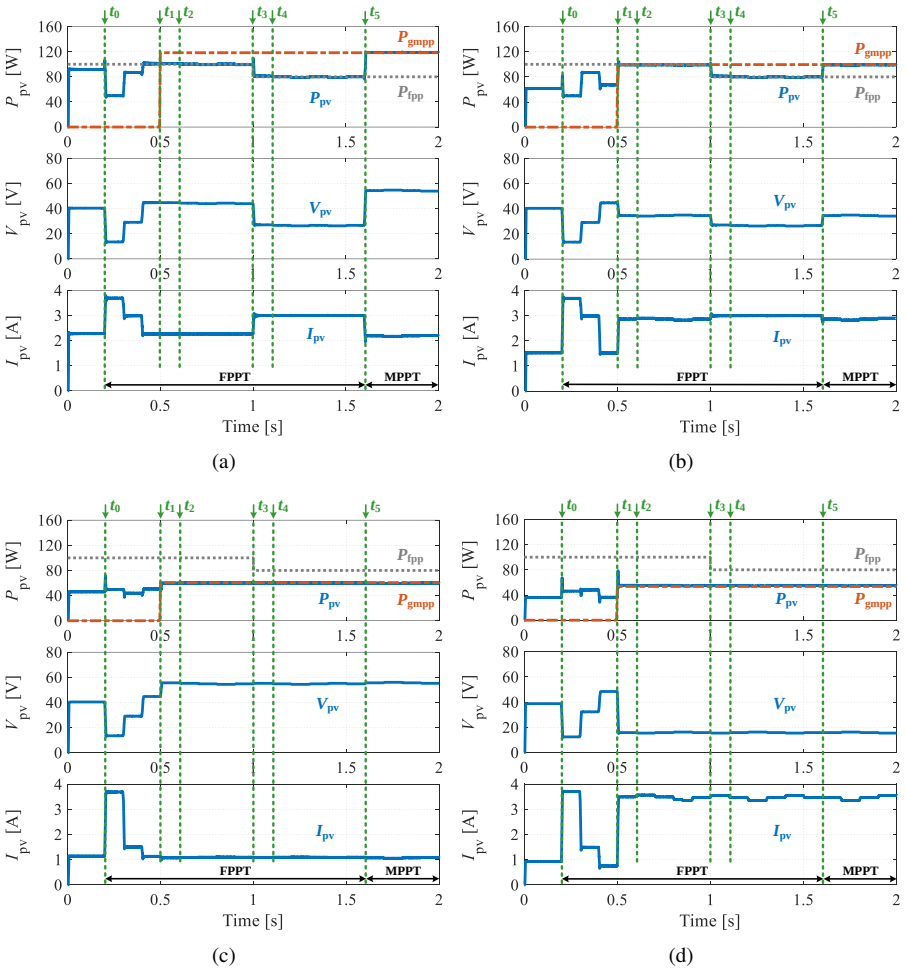

Fig. 12. Simulation results of proposed PST-FPPT algorithm under various three-peaks-PSCs. (a) Case 3-peaks-I. (b) Case 3-peaks-II. (c) Case 3-peaks-III. (d) Case 3-peaks-IV.

GFPPT in [23]. Generally, the PSCs variation has followed the trajectory of Case 3-peaks-I $\rightarrow$ Case 3-peaks-II $\rightarrow$ Case 3-peaks-III, and the $P_{\rm fpp}$ command is continuously maintained at 90W during the whole simulation. Meanwhile, the average tracking error ($T.E.$) in [15] is introduced to quantify the tracking efficiency, which is expressed as,

$$T.E. = \frac{\int |P_{\rm pv} - P_{\rm fpp}|}{\int |P_{\rm pv}|} \times 100\% \tag{17}$$

where $P_{\rm pv}$ is the actual PV power. TABLE IV summarized the benchmarking of different controls.

Fig. 16 demonstrated the simulation results of three investigated FPPT controls and the proposed PST-FPPT control under dynamic PSCs, and the corresponding operational trajectories are illustrated in Fig. 17. As demonstrated in Fig. 16(a) and 16(b), the FPPT controls in [13] and [18] are failed to track the FPP under Case 3-peaks-II. The corresponding trajectories, as shown in Fig. 17(a) and Fig. 17(b), demonstrated that the operation of [13] and [18] will trap at the right-most LMPP and unavailable to provide the FPPT capability, even though the available power is greater than the $P_{\rm fpp}$ command in this case. Subsequently, the remarkable $T.E.$ is leading by the trapping at LMPP, as 15.03% with [13] and 16.70% with [23]. Accordingly, implementing FPPT controls for uniform irradiance are averse to grid-support functionalities.

Unlike the previous FPPT controls for uniform irradiance, the GFPPT in [23] introduced a searching-skip mechanism to approach the $P_{\rm fpp}$ command, which could identify the shading scenario and ensure the PSC operation capability. As demonstrated in Fig. 16(c), the LMPP searching is activated once the PSC variation at time instant t_0 is detected. The LMPP is detected at t_1' but with a $P_{\rm pv}$ lower than the $P_{\rm fpp}$ command. According to the inherent mechanism of GFPPT, the operation point is reset to a preset value and begins to seek the FPP from the left-most module. At time instant t_1'', the operation point matching the $P_{\rm fpp}$ command is found, and the PV power extraction is restricted in subsequent operations. Here, the tracking time for FPP is $29T_{\rm p}$, as 2.9s in simulation. However, the $T.E.$ is increased to 20.09% resulting from sophisticated searching. At t_2, the shading scenario is changed to Case 3-peaks-III from Case 3-peaks-II. Similarly, seeking the LMPP is triggered once the PSC variation is detected. However, the operation points are finally concentrated on the GMPP after a tracking time of $21T_{\rm p}$, considering the available power in this case. Fig. 17(c) illustrated the operational trajectory of [23], which ensures the FPPT capability under PSCs. However, the curve scanning nature of [23] induced a certain amount of

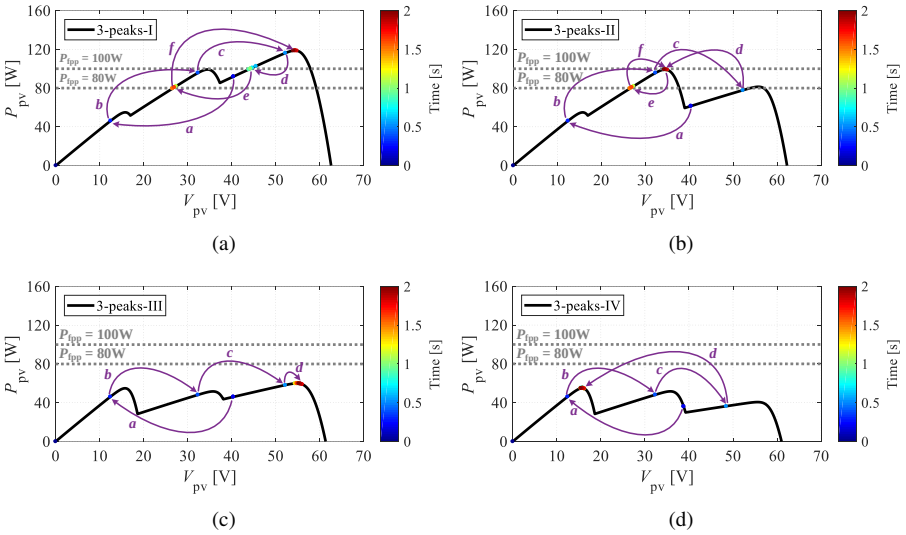

Fig. 13. Operational trajectory of proposed PST-FPPT algorithm under various three-peaks-PSCs. (a) Case 3-peaks-I. (b) Case 3-peaks-II. (c) Case 3-peaks-III. (d) Case 3-peaks-IV.

TABLE IV
BENCHMARKING OF DIFFERENT FPPT CONTROLS

Scenarios	Case 3-peaks-I to Case 3-peaks-II				Case 3-peaks-II to Case 3-peaks-III			
	Tracking Time	Tracking Error	FPP?	GMPP?	Tracking Time	Tracking Error	FPP?	GMPP?
[13]	11 T_p (Sim.) 9 T_p (Exp.)	15.03% 23.14%	No** No**	No No	1 T_p (Sim.) 1 T_p (Exp.)	52.35% 65.07%	No No	Yes Yes
[18]	1 T_p (Sim.) 1 T_p (Exp.)	16.70% 23.25%	No** No**	No No	1 T_p (Sim.) 1 T_p (Exp.)	55.47% 66.62%	No No	Yes Yes
[23]	29 T_p (Sim.) 18 T_p (Exp.)	20.09% 16.14%	Yes Yes	No No	21 T_p (Sim.) 10 T_p (Exp.)	68.22% 83.63%	No No	Yes Yes
This work	4 T_p (Sim.) 4 T_p (Exp.)	2.35% 3.79%	Yes Yes	No No	4 T_p (Sim.) 4 T_p (Exp.)	51.80% 61.74%	No No	Yes Yes

* Sim. - Simulation; Exp. - Experiment
**Trapped at local MPP (unable to track FPP)

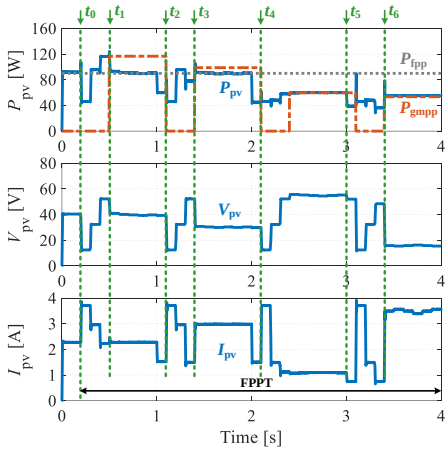

Fig. 14. Simulation results of proposed PST-FPPT algorithm under dynamic three-peaks PSCs.

sophisticated searching iterations, significantly reducing the control dynamics.

Fig. 16(d) illustrated the simulation results of the proposed PST-FPPT control under the same shading dynamics. Similar to the previous evaluation for the proposed control, the initial-

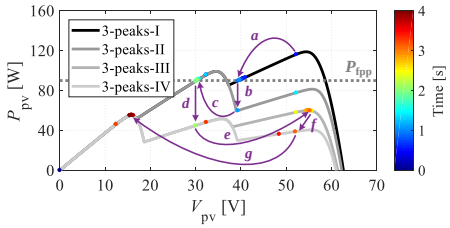

Fig. 15. Operational trajectory of proposed PST-FPPT algorithm under dynamic three-peaks PSCs.

ization process will be enabled to measure the representative PV currents at CCR once the shading variation is detected, as demonstrated in Fig. 17(d). Once the initialization is completed, the operation point would be directly switched to the FPP or GMPP at the adjacent perturbation interval following the relationship between the estimated available power and P_{fpp} command, which effectively enhanced the control dynamics. Notably, by implementing PST-FPPT control, the tracking time for the FPP or GMPP could effectively be constrained to $4T_{\mathrm{p}}$ in these three peaks shading scenarios.

The lowest $T.E.$ with the proposed control is mainly attributed to the minified initialized iterations for PSC detection

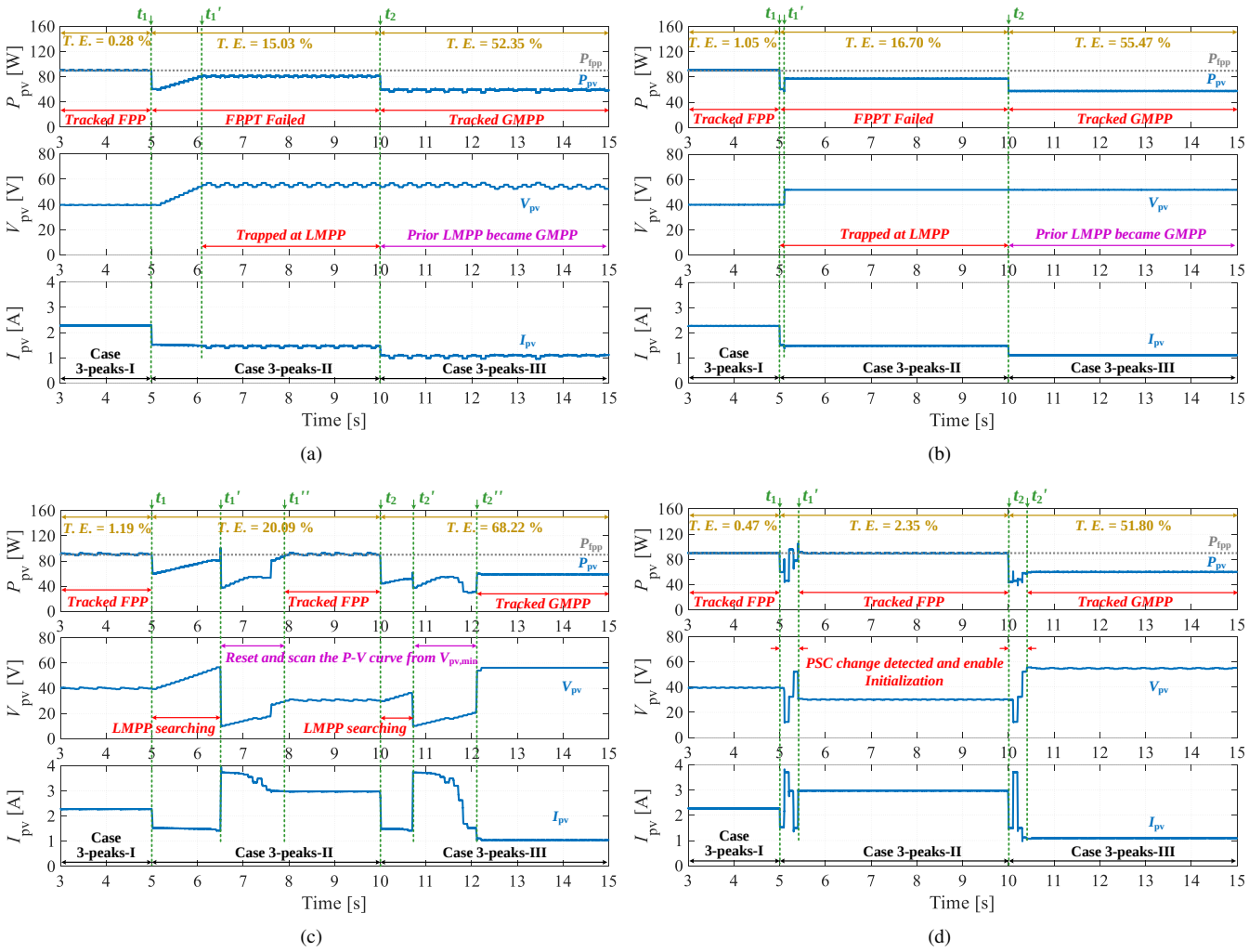

Fig. 16. Simulation comparison of different FPPT control schemes under dynamic PSCs. (a) Conventional FPPT in [13]. (b) Secant-based FPPT in [18]. (c) Global FPPT in [23]. (d) This work.

and direct operation point regulation-oriented FPP estimation. Meanwhile, the relatively high $T.E.$ with [23] originated from the sophisticated searching iterations for PSC detection but still performed a reliable operation capability under PSCs. Notably, the tracking time with [13], and [18] is not informative, considering their inapplicability under PSCs. Compared with the GFPPT in [23], the proposed PST-FPPT control could be reduced to a tracking time of $4T_{\rm p}$ from $29T_{\rm p}$ at PSC dynamics Case 3-peaks-I to Case 3-peaks-II, and $4T_{\rm p}$ from $21T_{\rm p}$ at PSC dynamics Case 3-peaks-II to Case 3-peaks-III, repetitively. Compared with other FPPT controls, the proposed PST-FPPT control outperformed in the PSC detection capability, fast-speed dynamic responses, and tracking error mitigation under environmental dynamics.

Here, the advances of the proposed control is validated by simulations and fair comparison.

IV. Experimental Validations

This section presents the experimental evaluation of the proposed PST-FPPT algorithm with various operational conditions. The experimental prototype is illustrated in Fig. 10(b). The specifications of the boost converter are the same as that used in the simulation, which are listed in TABLE III. A programmable DC supply, Chroma ATE-62050H-600S, was used to emulate the PV string with three series-connected MSX-60 modules. The control platform, dSPACE DS1104, is employed as the controller to implement the proposed control scheme and a sample interval of 0.3s. The electronic load, IT8514C+, was used and operated at constant voltage (CV) mode. The main components specifications of the boost converter were set the same as those used in simulations. The three-peaks shading scenarios in the simulation, as demonstrated in Fig. 11, are continuously employed in the experimental evaluation. Meanwhile, the experimental results under various five-peaks PSCs are provided to further prove the control effectiveness of the proposed PST-FPPT algorithm.

A. Steady Three-Peaks Shading Scenarios

Fig. 18 demonstrated the experimental results under three steady three-peaks shading scenarios but with $P_{\rm fpp}$ command variation and mode transition. Like the simulation, the proposed PST-FPPT algorithm is enabled at instant t_0. The $P_{\rm fpp}$ command is initially set at 100W and reduced to 80W at the time instant t_2. Once activated, the algorithm is operated at

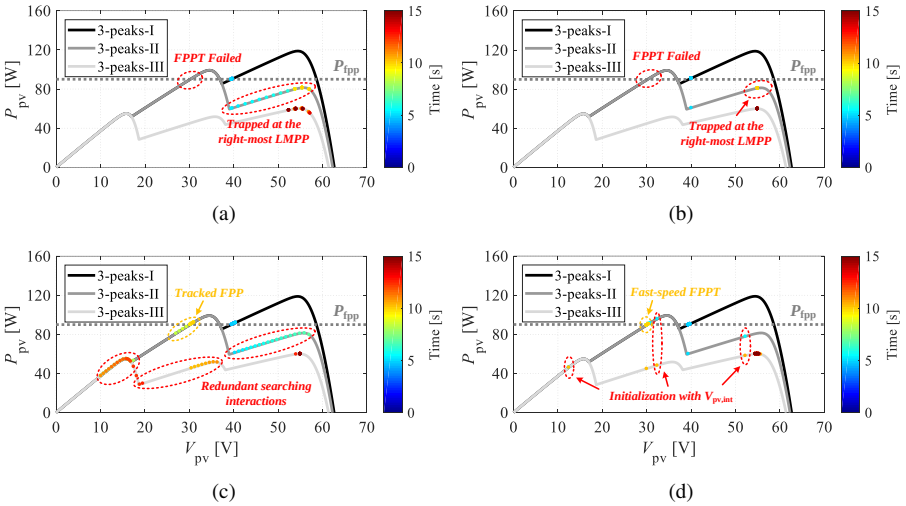

Fig. 17. Operational trajectory of different FPPT control schemes under dynamic PSCs. (a) Conventional FPPT in [13]. (b) Secant-based FPPT in [18]. (c) Global FPPT in [23]. (d) This work.

FPPT mode, then switched to MPPT mode at instant t_3 until the experiment is completed.

The experimental results with shading scenario Case 3-peaks-I are illustrated in Fig. 18(a). Between time instant t_0 and t_1, the proposed PST-FPPT is operated in the initialization process, which acquires the voltage-current pairs to detect the shading scenario. The initialization is completed at the time instant t_1. Then, the operation point will be directly regulated to the estimated FPP, guaranteeing the tracking speed. Subsequently, the operation point regulation will follow the (14) till t_2. At time instant t_2, the P_{fpp} command is changed to 80W. Then, the operation point is directly regulated to the region referred to the new power command in the next perturbation interval. The PV output power will oscillate around 80W based on P_{fpp} commend between t_2 and t_3. At t_3, the operation mode is switched to MPPT mode. The operation point is regulated to the GMPP directly by adopting the estimated V_{gmpp} as the reference voltage, resulting in a significant power increase once the MPPT mode is activated. After approaching the GMPP, the PST-FPPT algorithm continuously tracks the GMPP in the remaining operation.

The experimental results under Case 3-peaks-II are demonstrated in Fig. 18(b). Similarly, the operation PST-FPPT algorithm is enabled at t_0 and finished the initialization process at t_1. Notably, the available power of Case 3-peaks-II, as 99.18W, is lower than the initial P_{fpp} command 100W. Thus, the PV operation will be directly regulated to the GMPP in the next perturbation interval and continued with internal MPPT operation to maximize the power extraction. At time instant t_2, the P_{fpp} command is reduced to 80W, which is lower than the available power of Case 3-peaks-II. Subsequently, the PV operation point is moved from the GMPP to FPP to constrain the power output. At time instant t_3, the operation mode is switched to MPPT mode. Considering the operation between t_2 and t_3, the PV operation point is directly moved to the estimated GMPP and continued with maximum power extraction.

Fig. 18(c) demonstrated the experimental results under shading scenario Case 3-peaks-III. Similar to the operation in Case 3-peaks-II, the proposed PST-FPPT algorithm will track the GMPP after completing the initialization and the key points estimation. At t_2, the P_{fpp} command changed but is still larger than the estimated P_{gmpp}. The tracking point is continuously allocated at the GMPP with internal MPPT operation in FPPT mode. The mode transition occurs at time instant t_3, and tracking for GMPP is continued but with MPPT mode in the rest of the experiment.

Fig. 18(d) demonstrated the experimental results under shading scenario Case 3-peaks-IV. Similar to the operation under Case 3-peaks-III, the final operation point is allocated at GMPP for maximizing the power extraction during the FPPT mode operation between the time instant t_0 and t_3.

B. Dynamic Three-Peaks Shading Scenarios

The experimental validation for the proposed PST-FPPT algorithm under dynamic three-peaks PSCs is demonstrated in Fig. 19. The trajectory of shading scenarios variation is as in the simulation, and the P_{fpp} command is constantly set at 90W during the whole period. The proposed PST-FPPT algorithm is activated at t_0 and switched to the estimated FPP of Case 3-peaks-I at t_1, then regulates the output power to match the desired P_{fpp}. At time instant t_2, the shading scenario is changed to Case 3-peaks-II. Subsequently, the initialization process for PSC determination is reactivated and completed at time instant t_3. Based on the estimated available power, the operation point is moved to the FPP according to the FPP estimation strategy after t_3. At time instant t_4, the shading scenario is switched to Case 3-peaks-III, where the available power is lower than 90W. Thus, the PST-FPPT algorithm must yield the maximum available power. The operation point is directly switched to the estimated GMPP at t_5 based on the key point estimation to guarantee the tracking speed. Then, the shading scenario is changed to Case 3-peaks-IV at t_6. Similarly, the operation point is directly allocated at the GMPP to maximize the power extraction once the initialization is completed at t_7.

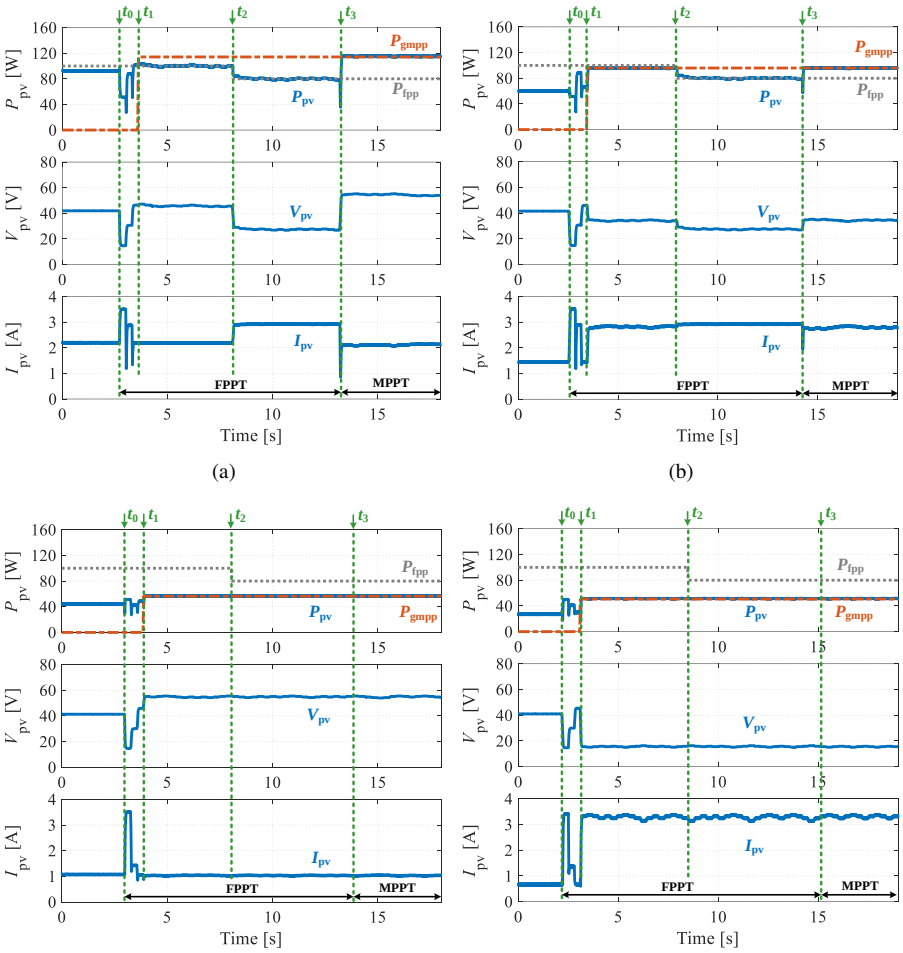

Fig. 18. Experimental results of proposed PST-FPPT algorithm under various three-peaks PSCs. (a) Case 3-peaks-I. (b) Case 3-peaks-II. (c) Case 3-peaks-III. (d) Case 3-peaks-IV.

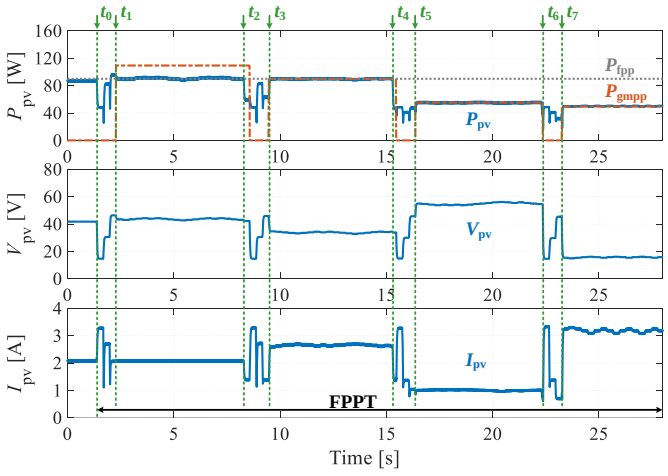

Fig. 19. Experimental results of proposed PST-FPPT algorithm under dynamic 3-peaks-PSCs.

C. Experimental Results under Five-Peaks PSCs

As demonstrated in Fig. 20, five five-peaks PSCs are introduced to validate the effectiveness of the proposed PST-FPPT algorithm under more complex shading scenarios. The irradiance levels of the investigated five-peaks PSC cases are listed as

- Case 5-peaks-I: 0.6kW/m^2, 0.225kW/m^2, 0.2kW/m^2, 0.175kW/m^2, 0.15kW/m^2
- Case 5-peaks-II: 0.9kW/m^2, 0.25kW/m^2, 0.2kW/m^2, 0.5kW/m^2, 0.1kW/m^2
- Case 5-peaks-III: 1.0kW/m^2, 0.7kW/m^2, 0.4kW/m^2, 0.3kW/m^2, 0.2kW/m^2
- Case 5-peaks-IV: 1.0kW/m^2, 0.6kW/m^2, 0.5kW/m^2, 0.3kW/m^2, 0.2kW/m^2
- Case 5-peaks-V: 1.0kW/m^2, 0.8kW/m^2, 0.6kW/m^2, 0.4kW/m^2, 0.2kW/m^2

The theoretical available power at GMPPs are 49.43W, 45.28W, 85.5W, 96.23W, and 115.8W, respectively.

Fig. 21 demonstrated the experimental results under the steady five-peaks PSCs. Like the three-peaks cases, the PST-FPPT algorithm is enabled at instant t_0. Subsequently, the proposed algorithm operates at FPPT mode until the MPPT mode is triggered at t_3. The P_{fpp} command is initially set at 100W, then, reduced to 80W at t_2. As illustrated in Fig. 21, since the initialization was completed at t_1, the PV output power could be successfully constrained at the desired level based on the relationship between the available power and P_{fpp} command during the FPPT mode operation. Meanwhile, the proposed PST-FPPT algorithm showed a reliable transient

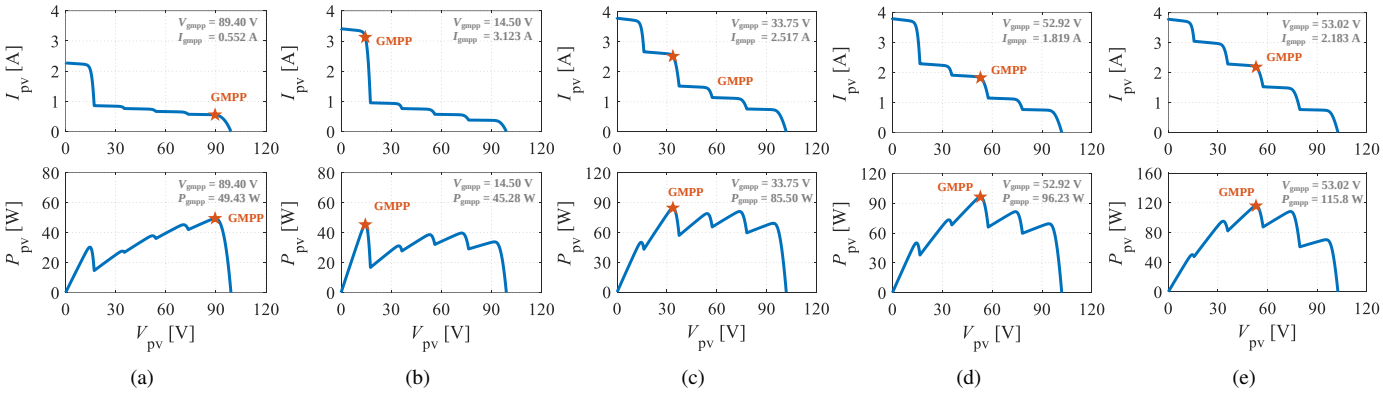

Fig. 20. Theoretical PV output characteristics under five-peaks PSCs. (a) Case 5-peaks-I. (b) Case 5-peaks-II. (c) Case 5-peaks-III. (d) Case 5-peaks-IV. (e) Case 5-peaks-V.

performance to the change of P_{fpp} command and mode transitions.

Fig. 22 demonstrated the experimental results under the dynamic five-peaks PSCs. The PSCs variations trajectory follows Case 5-peaks-I $\rightarrow$ Case 5-peaks-II $\rightarrow$ Case 5-peaks-III $\rightarrow$ Case 5-peaks-IV $\rightarrow$ Case 5-peaks-V. The P_{fpp} command is maintained at 90W during the whole experiment. The proposed PST-FPPT is enabled at time instant t_0, and the *Flag* signal is set at one in the remaining time. As shown in Fig. 22, the proposed control can successfully detect PSC variations. Subsequently, the initialization procedure is triggered to update the shading information. Accordingly, the operation point will be directly regulated to approach the point of P_{fpp} command or the GMPP after initialization, and the effectiveness of the proposed algorithm under five-peaks PSC variations is proved.

Here, the proposed PST-FPPT algorithm is validated by the experiments and performed a reliable response to the system dynamics on the P_{fpp} command changed and PSC variations.

D. Experimental Comparison under Dynamic Three-Peaks Shading Scenarios

To emphasize the control effectiveness, the experimental comparison under dynamic three-peaks PSCs is carried out. The numerical results are summarized in TABLE IV in terms of $T.E.$ and tracking time. Similar to the simulation comparison, the trajectory of PSC dynamics in the experimental comparison is following the sequence of Case 3-peaks-I $\rightarrow$ Case 3-peaks-II $\rightarrow$ Case 3-peaks-III, and the P_{fpp} command is maintained at 90W during the whole experiment. Fig. 23 demonstrated the experimental results of different FPPT methods. Similarly, the conventional FPPT [13] in Fig. 23(a) and the secant-based FPPT [18] in Fig. 23(b) are trapped at local MPP once the PSC is transited to Case 3-peaks-II at t_1, inducing the extreme large $T.E.$ of 23.14% and 23.25%, respectively. That is, the FPPT algorithms for uniform irradiance are unable to ensure the FPPT operation under PSC, degrading the grid-support capability. As demonstrated in Fig. 23(c), once the curve scanning process completed at $t_1^{''}$, the PV power is sufficiently restricted to the P_{fpp} command of 90W by implementing the GFPPT algorithm. However, the sophisticated searching mechanism dramatically reduced the tracking speed and induced a relatively large $T.E.$ of 16.4% during the operation with Case 3-peaks-II. Also, the inherent curve scanning reduced the tracking speed to the GMPP under Case 3-peaks-III. Fig. 23(d) illustrated the experimental of the proposed PST-FPPT algorithm. Generally, both the tracking speed and tracking error by adopting the proposed control is outperformed other FPPT algorithm.

Here, the advances of the proposed PST-FPPT algorithm are validated by experimental comparison.

V. Conclusion

In this paper, a partial-shading-tolerant FPPT algorithm is proposed with a key operation points estimation strategy, guaranteeing a sufficient balance between the tracking speed and computational burden. Generally, the proposed PST-FPPT control ensures the PSC detection capability by adopting a modified explicit PV model based on the samples from the initialization process. The proposed control could be developed for existing PVSs without additional hardware implementation by introducing the current-based irradiance estimation. The control effectiveness is validated under various operational conditions, including P_{fpp} regulation, mode transition, and PSC variations, based on a simplified boost converter-based PVS in both simulations and experiments. To highlight the advances of the PST-FPPT control, representative FPPT controls are introduced to a quantified comparison and summarized in TABLE IV. Generally, by analyzing the operational trajectory, the proposed control outperformed the shading tolerant capability of the conventional FPPT control [13], [18] for uniform irradiance and tracking speed to the curve scanning-based GFPPT method [23]. Notably, compared with the prior arts, the proposed PST-FPPT control required the minimum tracking time with a safeguard of tracking accuracy under the PSC dynamics. Moreover, the steady-state oscillations can be mitigated by optimizing the voltage regulation strategies, further increasing the tracking accuracy of the proposed method.

References

[1] Y. Yang, P. Enjeti, F. Blaabjerg, and H. Wang, "Wide-scale adoption of photovoltaic energy: Grid code modifications are explored in the distribution grid," *IEEE Ind. Appl. Mag.*, vol. 21, no. 5, pp. 21–31, Sep. 2015.

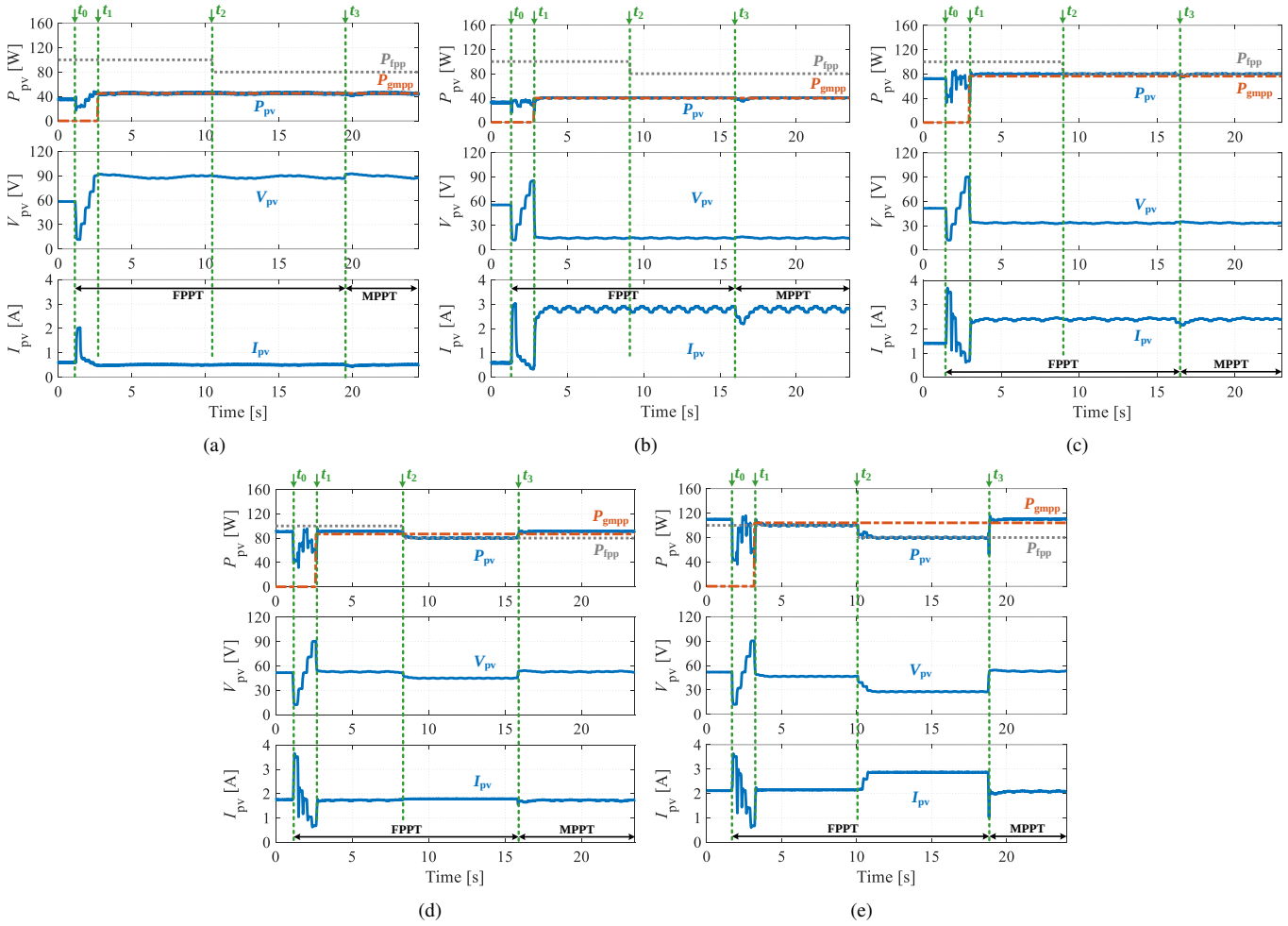

Fig. 21. Experimental results of proposed PST-FPPT algorithm under various five-peaks PSCs. (a) Case 5-peaks-I. (b) Case 5-peaks-II. (c) Case 5-peaks-III. (d) Case 5-peaks-IV. (e) Case 5-peaks-V.

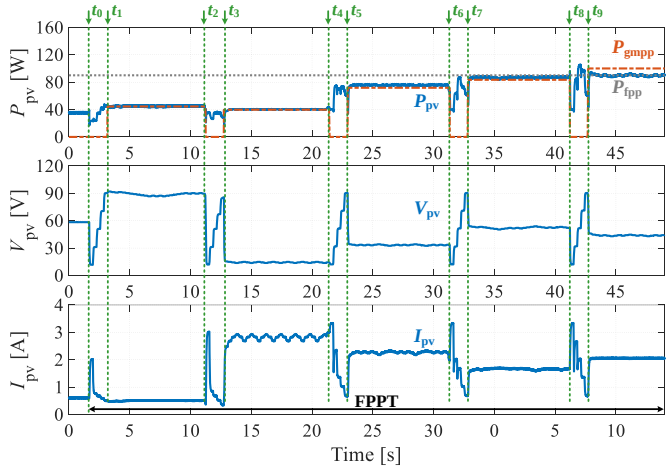

Fig. 22. Experimental results of proposed PST-FPPT algorithm under dynamic five-peaks PSCs.

[2] Y. Zhu, H. Wen, G. Chu, X. Wang, Q. Peng, Y. Hu, and L. Jiang, "Power-rating balance control and reliability enhancement in mismatched photovoltaic differential power processing systems," *IEEE Trans. Power Electron.*, vol. 37, no. 1, pp. 879–895, 2022.

[3] J. Fang, H. Li, Y. Tang, and F. Blaabjerg, "On the inertia of future more-electronics power systems," *IEEE J. Emerg. Sel. Top. Power Electron.*, vol. 7, no. 4, pp. 2130–2146, 2019.

[4] A. Khan, M. Hosseinzadehtaher, M. B. Shadmand, S. Bayhan, and H. Abu-Rub, "On the stability of the power electronics-dominated grid: A new energy paradigm," *IEEE Ind. Electron. Mag.*, vol. 14, no. 4, pp. 65–78, 2020.

[5] Y. Gu and T. C. Green, "Power system stability with a high penetration of inverter-based resources," *Proc. IEEE*, pp. 1–22, 2022.

[6] Energinet.dk, "Technical regulation 3.2.2 for pv power plants with a power output above 11 kw," *Energinet.dk, Errits, Denmark, Document No.: 14/17997-39, Tech. Rep.*, 2015.

[7] V. Gevorgian and B. O'Neill, "Advanced grid-friendly controls demonstration project for utility-scale pv power plants," NREL, Golden, CO, USA, Tech. Rep., Jan. 2016.

[8] North American Electric Reliability Corporation, "Frequency response and frequency bias setting reliability standard," *NERC standard BAL-003-1*, 2018.

[9] "Ieee standard for interconnection and interoperability of distributed energy resources with associated electric power systems interfaces," *IEEE Std 1547-2018 (Revision of IEEE Std 1547-2003)*, pp. 1–138, 2018.

[10] H. D. Tafti, G. Konstantinou, C. D. Townsend, G. G. Farivar, A. Sangwongwanich, Y. Yang, J. Pou, and F. Blaabjerg, "Extended functionalities of photovoltaic systems with flexible power point tracking: Recent advances," *IEEE Trans. Power Electron.*, vol. 35, no. 9, pp. 9342–9356, 2020.

[11] Q. Peng, Z. Tang, Y. Yang, T. Liu, and F. Blaabjerg, "Event-triggering virtual inertia control of pv systems with power reserve," *IEEE Trans. Ind. Appl.*, vol. 57, no. 4, pp. 4059–4070, 2021.

[12] Y. Zhu, H. Wen, Q. Bu, X. Wang, Y. Hu, and G. Chen, "An improved photovoltaic power reserve control with rapid real-time available power estimation and drift avoidance," *IEEE Trans. Ind. Electron.*, vol. 70, no. 11, pp. 11 287–11 298, 2023.

[13] H. D. Tafti, C. D. Townsend, G. Konstantinou, and J. Pou, "A multi-

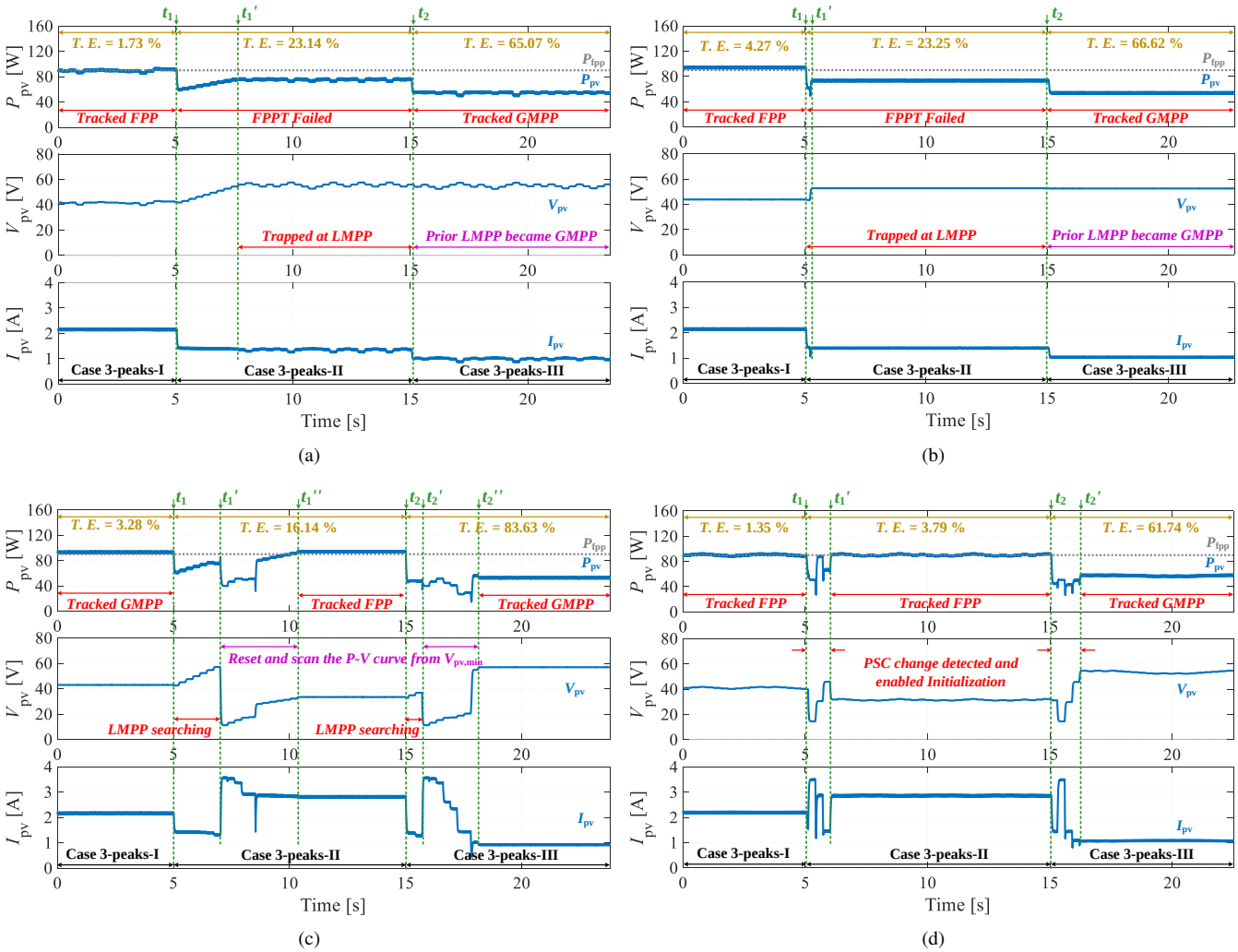

Fig. 23. Experimental comparison of different FPPT control schemes under dynamic PSCs. (a) Conventional FPPT in [13]. (b) Secant-based FPPT in [18]. (c) Global FPPT in [23]. (d) This work.

mode flexible power point tracking algorithm for photovoltaic power plants," *IEEE Trans. Power Electron.*, vol. 34, no. 6, pp. 5038–5042, 2019.

[14] A. Sangwongwanich, Y. Yang, and F. Blaabjerg, "High-performance constant power generation in grid-connected pv systems," *IEEE Trans. Power Electron.*, vol. 31, no. 3, pp. 1822–1825, 2016.

[15] H. D. Tafti, A. Sangwongwanich, Y. Yang, J. Pou, G. Konstantinou, and F. Blaabjerg, "An adaptive control scheme for flexible power point tracking in photovoltaic systems," *IEEE Trans. Power Electron.*, vol. 34, no. 6, pp. 5451–5463, June 2019.

[16] R. Gomez-Merchan, S. Vazquez, A. M. Alcaide, H. D. Tafti, J. I. Leon, J. Pou, C. A. Rojas, S. Kouro, and L. G. Franquelo, "Binary search based flexible power point tracking algorithm for photovoltaic systems," *IEEE Trans. Ind. Electron.*, vol. 68, no. 7, pp. 5909–5920, 2021.

[17] Y. Zhu, H. Wen, G. Chu, Y. Hu, X. Li, and J. Ma, "High-performance photovoltaic constant power generation control with rapid maximum power point estimation," *IEEE Trans. Ind. Appl.*, vol. 57, no. 1, pp. 714–729, 2021.

[18] A. Kumaresan, H. D. Tafti, N. K. Kandasamy, G. G. Farivar, J. Pou, and T. Subbaiyan, "Flexible power point tracking for solar photovoltaic systems using secant method," *IEEE Trans. Power Electron.*, vol. 36, no. 8, pp. 9419–9429, 2021.

[19] V. Paduani, H. Yu, B. Xu, and N. Lu, "A unified power-setpoint tracking algorithm for utility-scale pv systems with power reserves and fast frequency response capabilities," *IEEE Trans. Sustain. Energy*, pp. 1–1, 2021.

[20] E. I. Batzelis, S. A. Papathanassiou, and B. C. Pal, "Pv system control to provide active power reserves under partial shading conditions," *IEEE Trans. Power Electron.*, vol. 33, no. 11, pp. 9163–9175, Nov 2018.

[21] P. Verma, T. Kaur, and R. Kaur, "Power control strategy of PV system for active power reserve under partial shading conditions," *International Journal of Electrical Power & Energy Systems*, vol. 130, p. 106951, sep 2021.

[22] Z. Xie and Z. Wu, "A flexible power point tracking algorithm for photovoltaic system under partial shading condition," *Sustainable Energy Technol. Assess.*, vol. 49, p. 101747, feb 2022.

[23] H. D. Tafti, Q. Wang, C. D. Townsend, J. Pou, and G. Konstantinou, "Global flexible power point tracking in photovoltaic systems under partial shading conditions," *IEEE Trans. Power Electron.*, vol. 37, no. 9, pp. 11 332–11 341, 2022.

[24] H. Beltran, E. Bilbao, E. Belenguer, I. Etxeberria-Otadui, and P. Rodriguez, "Evaluation of storage energy requirements for constant production in pv power plants," *IEEE Trans. Ind. Electron.*, vol. 60, no. 3, pp. 1225–1234, 2013.

[25] H. D. Tafti, G. Konstantinou, J. E. Fletcher, L. Callegaro, G. G. Farivar, and J. Pou, "Control of distributed photovoltaic inverters for frequency support and system recovery," *IEEE Trans. Power Electron.*, vol. 37, no. 4, pp. 4742–4750, 2022.

[26] A. Sangwongwanich, Y. Yang, F. Blaabjerg, and H. Wang, "Benchmarking of constant power generation strategies for single-phase grid-connected photovoltaic systems," *IEEE Trans. Ind. Appl.*, vol. 54, no. 1, pp. 447–457, 2018.

[27] A. Sangwongwanich, Y. Yang, and F. Blaabjerg, "A sensorless power reserve control strategy for two-stage grid-connected pv systems," *IEEE Trans. Power Electron.*, vol. 32, no. 11, pp. 8559–8569, Nov 2017.

[28] E. I. Batzelis, I. A. Routsolias, and S. A. Papathanassiou, "An explicit pv string model based on the lambert w function and simplified mpp expressions for operation under partial shading," *IEEE Trans. Sustain.*

Energy, vol. 5, no. 1, pp. 301–312, 2014.
[29] M. L. Orozco-Gutierrez, J. M. Ramirez-Scarpetta, G. Spagnuolo, and C. A. Ramos-Paja, "A technique for mismatched pv array simulation," *Renew Energ*, vol. 55, no. jul., pp. 417–427, 2013.
[30] W. Xiao, W. G. Dunford, P. R. Palmer, and A. Capel, "Regulation of photovoltaic voltage," *IEEE Trans. Ind. Electron.*, vol. 54, no. 3, pp. 1365–1374, 2007.
[31] J. Kivimäki, S. Kolesnik, M. Sitbon, T. Suntio, and A. Kuperman, "Revisited perturbation frequency design guideline for direct fixed-step maximum power point tracking algorithms," *IEEE Trans. Ind. Electron.*, vol. 64, no. 6, pp. 4601–4609, 2017.
[32] R. Chinnappan, P. Logamani, and R. Ramasubbu, "Fixed frequency integral sliding-mode current-controlled MPPT boost converter for two-stage PV generation system," *IET Circuits, Devices & Systems*, vol. 13, no. 6, pp. 793–805, aug 2019.
[33] Z. Li, Z. Cheng, J. Si, S. Zhang, L. Dong, S. Li, and Y. Gao, "Adaptive power point tracking control of pv system for primary frequency regulation of ac microgrid with high pv integration," *IEEE Trans. Power Syst.*, vol. 36, no. 4, pp. 3129–3141, 2021.
[34] X. Li, Y. Zhu, H. Wen, Y. Du, and W. Xiao, "Reference-voltage-line-aided power incremental algorithm for photovoltaic gmppt and partial shading detection," *IEEE Trans. Sustain. Energy*, vol. 13, no. 3, pp. 1756–1770, 2022.
[35] N. Femia, G. Petrone, G. Spagnuolo, and M. Vitelli, *Power Electronics and Control Techniques for Maximum Energy Harvesting in Photovoltaic Systems*. CRC Press, jul 2017.
[36] H. Wang and F. Blaabjerg, "Reliability of capacitors for dc-link applications in power electronic converters—an overview," *IEEE Trans. Ind. Appl.*, vol. 50, no. 5, pp. 3569–3578, 2014.

Yinxiao Zhu (Graduate Student Member, IEEE) received the B.Eng. degree in microelectronic science and engineering from the Tianjin University of Technology and Education, Tianjin, China, in 2017. He received the M.Sc. (with Distinction) degree in sustainable energy technology and the Ph.D. degree in electrical and electronic engineering from the University of Liverpool, Liverpool, U.K., in 2019 and 2023, respectively. He is currently a Postdoctoral Fellow with the College of Electrical Engineering, Zhejiang University, Hangzhou, China.

His current research interests include the grid-integration of photovoltaic systems and control of power electronics, in particular, grid supportive controls and differential power processing technologies.

Huiqing Wen (Senior Member, IEEE) received the B.S. and M.S. degrees from Zhejiang University, Hangzhou, China, in 2002 and 2006, respectively, and the Ph.D. degree from the Chinese Academy of Sciences, Beijing, China, in 2009, all in electrical engineering. From 2009 to 2010, he was an Electrical Engineer with the GE (China) Research and Development Center Company, Ltd., Shanghai, China. From 2010 to 2011, he was an Engineer with the China Coal Research Institute, Beijing, China. From 2011 to 2012, he was a Postdoctoral Fellow with the Masdar Institute of Science and Technology, Abu Dhabi, United Arab Emirates. Since 2013, he has been with the Department of Electrical and Electronic Engineering, Xi'an Jiaotong-Liverpool University (XJTLU), Suzhou, China, where he is currently an Professor. He has authored or coauthored more than 50 peer-reviewed technical papers in leading journals. His research interests include renewable energy, electric vehicle, power electronics, microgrid, and power semiconductor devices.

Dr. Wen is the Associate Editor of IEEE Access, International Journal of Photoenergy, and Journal of Power Electronics. He is a Fellow of the Institution of Engineering and Technology (FIET).

Hossein Dehghani Tafti (Senior Member, IEEE) received the B.Sc. and M.Sc. degrees in electrical engineering and power system engineering from the Amirkabir University of Technology, Tehran, Iran, in 2009 and 2011, respectively, and the Ph.D. degree in electrical engineering from Nanyang Technological University, Singapore, in 2018. From January 2018 to April 2020, he was a Research Fellow at Nanyang Technological University, where he worked on the control of photovoltaic systems for grid support. From May 2020 to May 2021, he was a senior research associate with the University of New South Wales, Sydney, Australia, where he worked on the modelling and testing of commercial photovoltaic inverters. He is currently a research fellow at the Department of Electrical, Electronic and Computer Engineering, University of Western Australia, Perth, WA, where he is involved in designing a 1MVA energy storage system in conjunction with Magellan Power Pty Ltd.

His research interest includes the grid integration of renewable energy sources, in particular, photovoltaics and energy storage and the design and control of multilevel power converters.

Guangyu Wang (Graduate Student Member, IEEE) received the B.Eng degree in electrical engineering from the Northeast Electric Power University, Jilin, China, in 2018. He received the M.Sc degree in sustainable energy technology from Xi'an Jiaotong-Liverpool University, Suzhou, China, in 2021, where he is currently pursuing a doctorate in electrical and electronic engineering.

His research interests include control of DC/DC and DC/AC converter and three port photovoltaic energy storage inverter.

Qinglei Bu (Member, IEEE) received the B.Eng. (Hons) and Ph.D. degrees from the University of Liverpool, Liverpool, U.K., in 2017 and 2022, both in electrical engineering. He is currently a Lecturer in the Department of Mechatronics and Robotics, School of Advanced Technology, Xi'an Jiaotong-Liverpool University (XJTLU), Suzhou, China.

His research interests include bidirectional DC-DC converters, electric vehicles, and renewable power conversion systems.

Guanying Chu (Member, IEEE) received the B.S. and M.S. degrees in electrical and electronic engineering from the University of Sheffield, Sheffield, U.K., in 2014 and 2015, respectively. In 2021, he received Ph.D. degree in electrical and electronic engineering from the University of Liverpool, Liverpool, U.K.. He is currently a Lecturer in the Department of Electrical and Electronics Engineering, School of Advanced Technology at Xi'an Jiaotong-Liverpool University (XJTLU), Suzhou, China.

His current research interests include bidirectional DC–DC converter, photovoltaic generation system, and differential power processing technologies.

Haochen Shi (Member, IEEE) received the B.S. degree in electrical engineering from China Three Gorge University, Yichang, China, in 2014, the M.Eng. degree in electrical engineering from the University of Leicester, Leicester, U.K., in 2015, and the Ph.D. degree in electrical engineering from the University of Liverpool, Liverpool, U.K., in 2020. He is currently a Postdoctoral Fellow with the State Key Laboratory of Advanced Electromagnetic Engineering and Technology, School of Electrical and Electronic Engineering, Huazhong University of Science and Technology, Wuhan, China.

His research interests include bidirectional dc–dc converter, electrical vehicles, wireless power transfer, and renewable power conversion systems.

Yihua Hu (Senior Member, IEEE) received the B.S. degree in electrical engineering in 2003, and the Ph.D. degree in power electronics and drives in 2011, both at China University of Mining and Technology. Between 2011 and 2013, he was with the College of Electrical Engineering, Zhejiang University as a Postdoctoral Fellow. Between 2013 and 2015, he worked as a Research Associate at the power electronics and motor drive group, the University of Strathclyde. Between 2016 and 2019, he was a Lecturer in the Department of Electrical Engineering and Electronics, University of Liverpool (UoL). Between 2019 and 2023, he was a Reader and electrical engineering group head in the Electronics Engineering Department at The University of York (UoY). Currently, he is a Reader in the Department of Engineering at King's College London (KCL). He has published over 160 papers in IEEE Transactions journals. His research interests include renewable generation, power electronics converters and control, electric vehicle, more electric ship/aircraft, smart energy system and non-destructive test technology.

He is the associate editor of IEEE Transactions on Industrial Electronics, IET Renewable Power Generation, IET Intelligent Transport Systems and Power Electronics and Drives. He is a Fellow of Institution of Engineering and Technology (FIET) and a member of UK Young Academy. He was awarded Royal Society Industry Fellowship.

Lin Jiang (Member, IEEE) received the B.Sc. and M.Sc. degrees in electrical engineering from the Huazhong University of Science and Technology, Wuhan, China, and the Ph.D. degree in electrical engineering from the University of Liverpool, Liverpool, U.K., in 1992, 1996, and 2001, respectively. He was a Post-Doctoral Research Assistant with the University of Liverpool from 2001 to 2003 and a Post-Doctoral Research Associate with the Department of Automatic Control and Systems Engineering, University of Sheffield, Sheffield, U.K., from 2003 to 2005. He was a Senior Lecturer with the University of Glamorgan, Wales, U.K., from 2005 to 2007, and joined the University of Liverpool in 2007. He is currently a Reader with the Department of Electrical Engineering and Electronics, University of Liverpool, U.K..

His current research interests include control and analysis of power system, smart grid, and renewable energy.